Research Square

Preprints are preliminary reports that have not undergone peer review.
They should not be considered conclusive, used to inform clinical practice,
or referenced by the media as validated information.

Promoter Hypermethylation and Androgen Receptor Regulation Unveil Dual Oxidase 1 as a Tumor Suppressor in Prostate Adenocarcinoma

Abhik Saha

abhik.dbs@presiuniv.ac.in

Presidency University, Kolkata https://orcid.org/0000-0001-7390-4578

Subhadeep Nag

Presidency University, Kolkata

Purandar Sarkar

Presidency University, Kolkata

Samaresh Malik

Presidency University, Kolkata

Sourav Dutta

Presidency University, Kolkata

Joyanta Biswas

Presidency University, Kolkata

SK Ali

Presidency University, Kolkata

Souvik Alam

Presidency University, Kolkata

Abhishek Bardhan

Keya Basu

Institute of Post Graduate Medical Education And Research

Krishnendu Maiti

Amlan Ghosh

Arpita Konar

Somsubhra Nath

Presidency University https://orcid.org/0000-0001-8214-1218

Debanjan Mukhopadhyay

Presidency University https://orcid.org/0000-0002-8921-4106

Piyali Mukherjee

Article

Keywords:

Posted Date: May 21st, 2026

DOI: https://doi.org/10.21203/rs.3.rs-9621447/v1

License: This work is licensed under a Creative Commons Attribution 4.0 International License.
Read Full License

Additional Declarations: There is **NO** Competing Interest.

Promoter Hypermethylation and Androgen Receptor Regulation Unveil Dual Oxidase 1 as a Tumor Suppressor in Prostate Adenocarcinoma

Subhadeep Nag[1], Purandar Sarkar[1,5], Samaresh Malik[1,6], Sourav Dutta[1], Joyanta Biswas[1], SK Asif Ali[1,7], Souvik Alam[1], Abhishek Bardhan[2] Keya Basu[3], Krishnendu Maiti[4], Amlan Ghosh[2], Arpita Konar[1], Somsubhra Nath[1], Debanjan Mukhopadhyay[1], Piyali Mukherjee[1], Abhik Saha[1,*]

[1] Institute of Health Sciences, Presidency University, New Town, Kolkata, West Bengal, India

[2] Department of Life Sciences, Presidency University, College Street, Kolkata, West Bengal, India

[3] Department of Pathology, Institute of Post Graduate Medical Education and Research, Kolkata West Bengal, India

[4] Department of Urology, Institute of Post Graduate Medical Education and Research, Kolkata West Bengal, India

[5] Current address: Darjeeling Government College, Darjeeling, West Bengal, India

[6] Current address: University of Florida, Florida, USA

[7] Current address: Bar-Ilan University, Ramat Gan, Israel

* To whom correspondence should be addressed.

Email: abhik.dbs@presiuniv.ac.in; Tel: +91-9874924838

Keywords: DUOX1, NADPH Oxidase, Prostate Cancer, DNA-methylation, Androgen Receptor

Running Title: DUOX1 functions as a tumor-suppressor gene in prostate cancer

Abstract

Promoter hypermethylation of tumor suppressor genes (TSGs) is a hallmark of prostate cancer (PCa) development and holds promise as a diagnostic and prognostic biomarker. Through global methylation analysis of benign prostatic hyperplasia and PCa tissue samples, we identified dual oxidase 1 (DUOX1), a member of the NADPH oxidase family, as a methylation-driven TSG involved in PCa progression. Elevated DUOX1 expression is associated with improved disease-free and progression-free survival in PCa patients, emphasising its clinical relevance. Mechanistically, we show that *de novo* DNA methyltransferases (DNMT) -3A and -3B mediate DUOX1 promoter-hypermethylation, while the androgen receptor (AR) represses DUOX1 transcription by forming a negative chromosomal circuit through an enhancer-bound AR-H3K27ac-BRD4 axis. Genetic perturbations or pharmacological interventions with demethylating agents, anti-androgen therapies, or BET inhibitors relieve this repression, leading to increased DUOX1 expression. Functional restoration of DUOX1 in AR-positive PCa cells exhibited strong anti-proliferative and anti-metastatic effects by enhancing extracellular ROS production and reducing AR expression. Furthermore, DUOX1 re-expression selectively activated the cellular glucuronidation pathway, disrupting androgen signalling. Collectively, our findings establish DUOX1 as a methylation-driven, AR-regulated tumor suppressor and a promising biomarker for early diagnosis and targeted therapy in prostate adenocarcinoma.

Introduction

Prostate cancer (PCa) is a complex disease that affects millions of men globally and is the second most commonly diagnosed cancer among men [1,2]. If PCa is diagnosed and subsequently treated at an early stage, the overall survival of patients with low to intermediate risk of recurrence usually exhibits a favourable outcome [2]. Key genetic alterations in PCa include fusions of TMPRSS2 with ETS family genes, amplification of the c-Myc oncogene, deletion/mutation of several tumor suppressor genes (TSGs) - PTEN and TP53 and in advanced stages of PCa, mutation of the androgen receptor (AR) [3-7]. PCa is typically diagnosed by monitoring serum prostate-specific antigen (PSA) levels followed by transrectal ultrasound (TRUS) guided prostate biopsy [8]. However, these methods lack specificity and sensitivity, especially for detecting aggressive or recurrent PCa, leading to suboptimal management. Treatment for localized disease includes radical prostatectomy or ablative radiotherapy, while patients with advanced stages of PCa are treated with radiotherapy along with androgen deprivation therapy (ADT) with or without the combination of chemotherapy [9,10]. Importantly, advanced PCa often progresses despite androgen withdrawal, known as metastatic castration-resistant PCa (mCRPC), which results in significant morbidity and mortality [2,9]. Additionally, recurrent PCa remains another major problem largely due to lack of clinical symptoms and tumor-specific biomarkers during early stages of the disease. Identification and validation of early diagnostic biomarkers are thus imperative for effective PCa management.

Aberrant DNA methylation plays critical roles in PCa development [11,12]. Promoter hypermethylation of tumor suppressor genes (TSGs) has emerged as a promising mechanism for diagnostic and prognostic biomarker discovery [11]. Restoring the expression of these genes offers potential therapeutic strategies, particularly for aggressive PCa. Several methylation-driven TSGs implicated in PCa risk have been identified. These include GSTP1, RARB, CDKN2A, RASSF1A, SCGB3A1, APC and HIF3A [13-19]. In addition, many genome-wide association studies (GWAS) along with large integrative multi-omics data identified novel CpG sites and genes, contributing to PCa development [20-22].

Dual oxidase 1 (DUOX1), a member of the NADPH oxidase (NOX) family, is involved in diverse biological processes, including reactive oxygen species (ROS) generation, hormone synthesis, and cell proliferation [23]. The NOX family encompasses seven members – NOX1-5, and DUOX1-2 [23]. In addition to the well-characterized NOX-domain accountable for ROS production, DUOX proteins contain an extracellular peroxidase domain, sharing sequence homology to myeloperoxidase and lactoperoxidase enzymes [23]. Altered ROS production has been implicated in numerous pathologic conditions [24]. Increased ROS levels largely contribute to cancer progression and apart from mitochondrial ROS, NOXs represent the main sources for ROS production in redox regulation of cell signalling cascades [23]. Notably, most of the NOXs are significantly elevated in multiple cancers [25-27], elucidating the increased ROS levels in tumor background compared to the normal counterpart. Unlike other NOXs, DUOX1 expression along with its maturation factor DUOXA1 is frequently depleted due to promoter hypermethylation in several solid cancers [28-31]. For example, DUOX1 silencing promotes epithelial-to-mesenchymal transition (EMT), cancer stem cell properties, and invasiveness in lung carcinoma [30]. Moreover, elevated DUOX1 expression in hepatocellular carcinoma is strongly correlated with overall patients' survival [28]. However, DUOX1 depletion in various cancers seems paradoxical since cancer cells are usually characterized by elevated ROS levels [23]. Indeed, several studies suggested a potential role for DUOX1-derived H_2O_2 in some cancers. For example, one study demonstrated that ionizing radiation mediated DUOX1 induction plays a crucial role in radio-induced thyroid cancer [32]. Although the significance is not clear, another study demonstrated that ROS can maintain the expressions of DUOX1 and DUOX2 in human neuroblastoma cells [33]. DUOX1 may therefore exhibit distinct functions in tumorigenesis, contingent upon specific cell type and stage of cancer. To date, there is limited and inconsistent evidence directly linking NOX family members, particularly DUOX1, to PCa pathogenesis. For instance, one study reported that DUOX enzymes contribute to maintaining intrinsic ROS levels in PC3 cells, thereby promoting AKT signalling and resistance to apoptosis [34]. Conversely, a separate report demonstrated elevated DUOX1 expression

in DU145 cells, although such high expression is also detected in the immortalized prostate epithelial cell lines, EP156T and RWPE1 [35].

The present study was initiated with an aim to identify methylation-driven TSGs associated with PCa risk. Our genome-wide methylation analysis identified DUOX1 as a novel candidate TSG with significantly elevated promoter hypermethylation in PCa compared to benign prostatic hyperplasia (BPH) patients' tissue biopsy samples. Increased DUOX1 expression predicts a favorable prognosis in PCa patients. Besides promoter hypermethylation, DUOX1 is transcriptionally repressed by an enhancer-bound AR-H3K27ac-BRD4 axis, coordinating a negative chromosomal loop. Restoration of DUOX1 expression displays robust anti-proliferative and anti-metastatic effects through excessive ROS production and downregulating AR expression. Moreover, re-expression of DUOX1 deregulates glucuronidation, a major metabolic pathway that controls active androgen levels in the prostate. Collectively, we mechanistically validate DUOX1's role as an AR-regulated and methylation-driven TSG, offering insights into its potential as a biomarker for early diagnosis and targeted therapy in PCa management.

Materials and Methods

Ethics statement

The study was approved by the Institutional Review Board of Institute of Post Graduate Medical Education & Research (IPGME&R), Kolkata, India (Memo No. Inst/IEC2015/473). Written informed consent was obtained from all participants and all methods in this study were performed in accordance with the ethical principles founded in the Declaration of Helsinki.

Subject recruitment and specimen collection

A standard TRUS-guided 12-core prostate biopsy with subsequent histopathological analysis was carried out in patients with abnormal serum PSA level (>4.0 ng/ml). All cases included were newly diagnosed patients without any prior treatment before surgery. Individuals with clinical evidence of prostatic lesions receiving radiotherapy and/or undergoing androgen deprivation therapy (ADT) were excluded. 'Discovery cohort' containing 8 benign prostatic hyperplasia (BPH) and 8 PCa formalin-fixed paraffin-embedded (FFPE) tissue biopsy samples were subjected to Methyl Array. 'Validation cohort' containing freshly frozen 8 BPH and 8 PCa tissue biopsy samples were subjected to RNA isolation followed by qPCR analysis. Clinical characteristics of both sample cohorts are described in Table S1.

Nucleic acid extraction from tissue samples

FFPE tissue biopsy samples from the 'discovery cohort' were obtained as 10 µm sections mounted on non-charged glass slides. Genomic DNA was extracted using the standard phenol-chloroform method, as previously described [36]. The quality and quantity of the extracted DNA were assessed by agarose gel electrophoresis and by measuring the A260/280 ratio using the Synergy H1 Multimode Microplate Reader (BioTek Instruments, Inc., USA). ~300 ng of DNA from each sample was used for genome-wide methylation analysis.

For the 'validation cohort', needle biopsy tissues were homogenized, and total RNA was isolated using the RNeasy Mini Kit (Qiagen) according to the manufacturer's instructions.

Global methylation profiling

Genome-wide DNA methylation profiling of all 16 samples was performed using the Infinium MethylationEPIC v2.0 BeadChip (Illumina, Inc.) following bisulfite conversion with the EZ DNA Methylation Kit (Zymo Research). The Infinium MethylationEPIC v2.0 BeadChip is an array-based platform that interrogates over 850,000 CpG methylation sites across the genome. Following bisulfite treatment, DNA samples were amplified, fragmented, purified, and hybridized onto the EPIC BeadChip according to the manufacturer's instructions. The arrays were subsequently washed and scanned using the Illumina HiScan System. Signal intensities and raw methylation β-values were extracted using Illumina's GenomeStudio software. Quality control filtering was applied to remove probes with signals derived from two or fewer beads or with detection p-values greater than 0.01. Signal intensities were then normalized, and background correction was performed using negative control probes to obtain reliable methylation β-values. The β-value for each CpG site was calculated as the ratio of the methylated probe intensity to the total probe intensity, ranging from 0 (completely unmethylated) to 1 (fully methylated). All downstream data processing and analysis were conducted using the RnBeads package in R. Raw methyl array data along with the corresponding downstream analyses are presented in Dataset S1.

Bioinformatics analysis

All raw sequencing reads generated from high-throughput sequencing pipelines were initially assessed for quality using FastQC (http://www.bioinformatics.babraham.ac.uk), which confirmed the absence of significant quality issues. All publicly available datasets used in this study are tabulated in Table S2.

The Cancer Genome Atlas (TCGA) data analysis: 450K DNA-methylation and RNA-Seq data from TCGA database were analyzed using Shiny Methylation Analysis Resource Tool (SMART; http://www.bioinfo-

zs.com/smartapp/) and the University of ALabama at Birmingham CANcer data analysis portal (UALCAN; https://ualcan.path.uab.edu/).

Bulk RNA-Sequencing (RNA-Seq) data analysis: Raw FASTQ files of transcriptomic datasets were downloaded using unique SRR accession numbers and processed via the Galaxy webserver (https://usegalaxy.org/). Downstream analyses were performed using appropriate tools available within the platform. Data visualization was carried out using GraphPad Prism v8 and Microsoft Excel.

Single-cell RNA-Seq (scRNA-Seq) data analysis: Publicly available scRNA-seq datasets were processed using the Galaxy webserver. Raw expression matrices, along with feature and barcode files, were imported and converted into h5ad format for downstream analysis. Quality control filtering excluded low-quality cells based on low gene counts, high mitochondrial transcript proportions, or abnormal total read counts. The filtered data were normalized and log-transformed, followed by identification of highly variable genes. Dimensionality reduction was performed, and Uniform Manifold Approximation and Projection was used for visualization. Cell clustering was conducted using the Leiden algorithm based on a nearest-neighbor graph. Differential gene expression analysis was performed using the Wilcoxon rank-sum test, with p-values adjusted using the Benjamini-Hochberg procedure. Cluster-specific marker genes were identified and visualized using UMAP projections.

Chromatin immunoprecipitation sequencing (ChIP-Seq) data analysis: Raw FASTQ files from ChIP-Seq experiments were extracted from SRA files and aligned to the human reference genome (*Homo sapiens* GRCh37) using default parameters. Resulting BAM files were analyzed for peak calling using MACS2. Processed data were visualized using the Integrative Genomics Viewer (IGV, https://igv.org/).

DepMap cell line data analysis: Gene expression data for PCa and immortalized prostate epithelial cell lines were obtained from the DepMap Expression Public 25Q3 (https://depmap.org/portal/). Correlation analyses were performed using GraphPad Prism v8. The extracted gene expression profiles from the DepMap dataset are provided in Table S3.

450K methylation array data analysis: DNA methylation datasets were retrieved from multiple studies available in the NCBI Gene Expression Omnibus (GEO) portal

(https://www.ncbi.nlm.nih.gov/geo/). β-values were extracted directly from series matrix files. Relevant probes corresponding to genes or CpG sites of interest were selected, and data were compiled using Microsoft Excel. Graphical representations were generated using GraphPad Prism v8.

Bisulfite sequencing data analysis: Publicly available bisulfite sequencing datasets were reanalyzed using the ChIP-Atlas (https://chip-atlas.org/). Data were processed through the platform's standard pipeline to generate genome-wide DNA methylation profiles. Differentially methylated regions were identified using default thresholds, and results were visualized using IGV.

Microarray data analysis: Microarray datasets were obtained from the NCBI GEO portal. Normalized expression values were extracted from series matrix files, and probes corresponding to genes of interest were selected. Expression data were compiled and visualized using GraphPad Prism v8.

Cell lines

LNCaP (CRL-1740), DU145 (HTB-81), and MyC-CaP (CRL-3255) were obtained from American Type Culture Collection. Lenti-X 293T cells were procured from Takara Bio Inc. LNCaP cells were cultured in RPMI-1640 medium (Gibco), whereas DU145, MyC-CaP, and Lenti-X 293T cells were maintained in DMEM (Gibco). All cell lines were grown in media supplemented with 10% fetal bovine serum (FBS; Gibco/Avantor) and 1% penicillin–streptomycin solution (Gibco), and maintained at 37^0C in a humidified incubator with 5% CO_2. All cell lines were routinely screened for mycoplasma contamination using the LookOut Mycoplasma qPCR Detection Kit. Cell line authentication was performed by short tandem repeat (STR) profiling. Detailed information on all cell lines used in this study is provided in Table S4.

Western blot (WB) analysis

~2.0 × 10^7 cells from each experiment were harvested, washed with ice-cold 1× PBS (Gibco/Invitrogen), and lysed in 500 µL RIPA buffer (Thermo Fisher Scientific) supplemented with 1× protease inhibitor cocktail (Abcam). Cell lysates were subjected to intermittent vortexing for 15 s at 5

min intervals to ensure efficient lysis. Total protein concentration was determined using the Bradford assay (Bio-Rad). Protein samples were then mixed with 4× Laemmli buffer (Bio-Rad) and denatured by boiling at 95^0C for 7 min. Equal amounts of protein were resolved by SDS-PAGE and subsequently transferred onto nitrocellulose membranes (Bio-Rad). Membranes were blocked with 5% non-fat milk in 1× TBS and then washed with 1× TBST. The blots were incubated overnight at 4^0C with appropriate primary antibodies. The following day, membranes were washed with 1× TBST and incubated with appropriate infrared-tagged/DyLight secondary antibodies (Thermo Fisher Scientific) for 1 hour at room temperature. After final washes with 1× TBST, protein bands were visualized and quantified using the Odyssey Infrared Imaging System (LI-COR Biosciences). A complete list of primary and secondary antibodies used in this study is provided in Table S5.

Real-time quantitative PCR (qPCR)

~1.0×10^7 cells from each experimental condition were harvested for total RNA isolation using PureZOL RNA Isolation Reagent (Bio-Rad) according to the manufacturer's instructions. Approximately 1 µg of RNA was reverse transcribed into cDNA using the iScript cDNA Synthesis Kit (Bio-Rad). The quality and quantity of nucleic acids were assessed using the Synergy H1 Multimode Microplate Reader (BioTek Instruments). qPCR was performed using iTaq Universal SYBR Green Supermix (Bio-Rad) on the CFX Connect Real-Time PCR Detection System (Bio-Rad). Unless otherwise specified, each reaction was performed in triplicate. Relative gene expression levels were calculated using the $2^{-\Delta\Delta CT}$ method and normalized to internal control genes (GAPDH, B2M or ACTB). All experiments included technical triplicates and were repeated at least three times independently. A complete list of primers used for qPCR analysis is provided in Table S6.

Cell viability assays

Cell viability was assessed using the 3-(4,5-dimethylthiazol-2-yl)-2,5-diphenyltetrazolium bromide (MTT) dye reduction assay (Sisco Research Laboratories). Briefly, ~1×10^4 cells suspended in 100 µL

medium were seeded into 96-well tissue culture plates (Corning Inc.) and treated with the indicated compounds – 0-8 µM DNA methylation inhibitor 5-Aza-2'-deoxycytidine (Aza; Merck Sigma-Aldrich), 3 µM DNMT3A inhibitor DY-46-2 (MedChemExpress), 1 µM BET bromodomain inhibitor JQ1 (MedChemExpress), or 1 µg/mL doxycycline hyclate (DOX; MedChemExpress) for induction of DUOX1 expression. 24-72 h post-treatment, 10 µL of 5 mg/mL MTT solution was added to each well, followed by incubation for an additional 4 hours at 37^0C. The medium was then carefully removed, and the resulting formazan crystals were dissolved in 150 µL DMSO with incubation for 15 min. Absorbance was measured at 570 nm using a microplate reader (Thermo Fisher Scientific). Each experiment was performed in triplicate. After background subtraction, results were expressed as mean cell viability.

Colony formation assays

~5 × 10^4 LNCaP and DUOX1 stably expressing LNCaP (LNCaP-DUOX1) or MyC-CaP (MyC-CaP-DUOX1) cells were seeded into 6-well tissue culture plates (Corning Inc.) containing complete media and incubated at 37^0C. The culture medium was replaced every 48 h with 4 µM Aza for LNCaP cells, or with 1 µg/mL DOX for LNCaP-DUOX1 and MyC-CaP-DUOX1 cells, in the presence or absence of 5 mM N-acetyl-L-cysteine (NAC; Merck Sigma-Aldrich). After two weeks of incubation, cells were fixed with 4% paraformaldehyde (Merck Sigma-Aldrich) at room temperature and stained with 0.5% (w/v) crystal violet solution (Merck Sigma-Aldrich). Plates were scanned using the Odyssey CLx Imaging System, and relative colony numbers were quantified using ImageJ. For additional quantification, stained colonies were destained with 10% (v/v) acetic acid, and absorbance was measured at 550 nm.

Measurement of intracellular reactive oxygen species (ROS)

~1 × 10^4 LNCaP cells were seeded into 96-well tissue culture plates and either left untreated (DMSO control) or treated with 4 µM Aza or 1 µg/ml DOX for 48 h. For androgen deprivation experiments, LNCaP cells were serum-starved for 48 h in medium supplemented with 5% charcoal-stripped serum (CSS; Thermo Fisher Scientific), followed by treatment with 20 µM AR antagonists –enzalutamide

(MDV3100; Enza; MedChemExpress) or bicalutamide (Bica; Merck Sigma-Aldrich), for 72 h. LNCaP cells stably transfected with a DUOX1 expression construct under a DOX-inducible promoter were treated with 1 µg/ml DOX for 48 h. Intracellular ROS levels were measured using the cell-permeable fluorescent probe 2',7'-dichlorofluorescein diacetate ($DCFH_2$-DA; MedChemExpress). Following incubation with 20 µM $DCFH_2$-DA for 30 minutes at 37^0C, fluorescence intensity was measured using the Synergy H1 Multimode Microplate Reader (BioTek Instruments), with excitation at 485 nm and emission at 528 nm. All experiments were performed with at least three independent biological replicates.

Lentivirus mediated knockdown (KD) of DNMT3A

Lenti-X 293T cells were transfected with pGIPZ-Sh-Control or pGIPZ-Sh-DNMT3A constructs along with lentiviral packaging plasmids pMDG and psPAX2 using the calcium phosphate ($CaPO_4$) transfection method, as previously described [37]. The transfection medium was replaced with complete growth medium after 12 h. At 48 h post-transfection, lentivirus-containing supernatants were collected, filtered through a 0.45 µm membrane (Corning), and used to transduce ~5×10^5 LNCaP cells in the presence of 8 µg/mL polybrene (Merck Sigma-Aldrich) to enhance transduction efficiency. Following transduction, cells were selected with 1 µg/mL puromycin (Merck Sigma-Aldrich) in complete RPMI-1640 medium for 7 days to establish stable KD LNCaP cells. The oligonucleotides used for DNMT3A knockdown are listed in Table S6.

ChIP-qPCR analysis

ChIP-qPCR was performed as previously described [37]. Briefly, 1×10^7 cells were cross-linked with 1% (v/v) formaldehyde (Merck Sigma-Aldrich) for 10 min at room temperature. Cross-linking was quenched by adding 125 mM glycine (Bio-Rad) for 5 min at room temperature. Cells were washed with ice-cold 1× PBS and lysed in lysis buffer (50 mM Tris-HCl pH 8.1, 10 mM EDTA, 1% SDS, and 1× protease inhibitor cocktail). Chromatin was sheared to an average size of ~200-500 bp using the

Bioruptor Plus Sonicator (Diagenode) with 20 cycles of 30 s pulses on ice. A 10% aliquot of the sheared chromatin was saved as input control. The remaining chromatin was diluted 10-fold in immunoprecipitation (IP) dilution buffer (16.7 mM Tris-HCl pH 8.1, 1.2 mM EDTA, 167 mM NaCl, 1.1% Triton X-100, 0.01% SDS, and 1× protease inhibitor cocktail) and subjected to IP using 5 µg of specific antibodies or corresponding IgG controls with magnetic Protein A/G beads (Abcam). Following immunoprecipitation, complexes were sequentially washed with low-salt, high-salt, LiCl, and TE buffers. Protein-DNA complexes were then eluted in elution buffer (100 mM $NaHCO_3$, 1% SDS) at 55^0C for 15 min. Cross-links were reversed by treatment with proteinase K (New England Biolabs). ChIP DNA was purified using the QIAquick PCR Purification Kit (Qiagen) and subjected to qPCR analysis. Data were normalized to input DNA and expressed as a percentage of input. Primer sequences used for ChIP-qPCR are provided in Table S6.

Transient transfection

For WB and luciferase based promoter analysis assays, LNCaP or DU145 cells were seeded at ~50% confluency in 100 mm tissue culture dishes or 12-well plates. Cells were transfected with the appropriate plasmids using jetOPTIMUS transfection reagents (Polyplus Transfection) according to the manufacturer's instructions. Cells were harvested 36-48 h post-transfection and processed for protein expression analysis or luciferase activity assays.

sgRNA-mediated gene knockout (KO)

Single guide RNAs (sgRNAs) targeting AR, BRD4, and FOXA1 were designed using the Synthego CRISPR Design Tool (https://www.synthego.com/products/bioinformatics/crispr-design-tool) and subsequently synthesized by Integrated DNA Technologies. The oligonucleotides were annealed and cloned into the *Bbs*I restriction site of the pSpCas9(BB)-2A-Puro (PX459) V2.0 plasmid (Addgene). LNCaP cells were transfected with sgRNA-expressing plasmids using jetOPTIMUS (Polyplus Transfection) according to the manufacturer's protocol. Stable KO LNCaP cells were established by

selection with 1 µg/mL puromycin (Merck Sigma-Aldrich) in complete RPMI-1640 medium for 7 days. KO efficiency was validated by WB analysis. The oligonucleotide sequences used for targeting AR, BRD4 and FOXA1 are provided in Table S6.

Androgen stimulation and deprivation

For androgen stimulation, LNCaP cells were serum-starved for 48 h in phenol red-free RPMI-1640 medium (Thermo Fisher Scientific) supplemented with 5% charcoal-stripped serum (CSS), followed by stimulation with 10 nM 5α-dihydrotestosterone (DHT; Merck Sigma-Aldrich) for 72 h. For androgen deprivation experiments, LNCaP cells were serum-starved under the same conditions and subsequently treated with 20 µM Enza or Bica for 72 h.

Confocal microscopy

LNCaP cells grown on glass coverslips in 24-well culture plates were fixed with 4% paraformaldehyde (Merck Sigma-Aldrich). Cells were washed with 1× PBS, permeabilized with 0.1% Triton X-100 (Merck Sigma-Aldrich) in PBS for 10 min, and blocked with 5% BSA (Bio-Rad) in PBS at room temperature for 1 h. Following blocking, cells were incubated with appropriate primary antibodies overnight at 4^0C. After washing with 0.05% Tween-20 in PBS (PBST), cells were incubated with Alexa Fluor-conjugated, species-specific anti-mouse or anti-rabbit secondary antibodies (Thermo Fisher Scientific) for 1 h at room temperature. Nuclei were counterstained with 4',6-diamidino-2-phenylindole (DAPI; Bio-Rad) for 30 min. Cells were washed three times with PBST and mounted using antifade mounting medium (Merck Sigma-Aldrich). For mitochondrial reactive oxygen species (ROS) analysis, ~5 × 10^4 LNCaP-DUOX1 cells were cultured to ~70% confluency on 35 mm glass-bottom dishes (Thermo Fisher Scientific) and treated with 1 µg/ml DOX for 48 h. For live-cell imaging, Hoechst 33342 and MitoSOX Red (Thermo Fisher Scientific) were used according to the manufacturer's instructions. Fluorescence images were acquired using the Leica DMi8 Confocal Microscope and processed with Leica Application Suite X (Leica Microsystems). In selected experiments, fluorescence intensities were quantified using

ImageJ. A complete list of primary and secondary antibodies used for immunofluorescence (IF) analysis is provided in Table S5.

Generation of constructs for promoter analysis

AR-binding (chr15: 45139468–45140299; 832 bp) containing single androgen response element (ARE) and non-binding (chr15: 45130940–45132013; 1074 bp) regions within the DUOX1 locus were amplified and cloned into the pGL3 promoter vector (Addgene) at the *Mlu*I and *Bgl*II restriction sites. A mutated ARE was generated by assembly PCR and cloned into the pGL3 promoter vector using the same restriction sites. In addition, a DNA-binding domain (DBD) mutant of AR (ARΔDBD) was generated by assembly PCR and subcloned into the pA3F expression vector using *Bam*HI and *Eco*RI restriction sites. All primers were synthesized by Integrated DNA Technologies. Sequences of the constructs were verified by Sanger dideoxy sequencing performed by Eurofins Genomics India. Primer sequences used for cloning and mutagenesis are provided in Supplementary Table S6. Details of all constructed plasmids are provided in Table S7.

Luciferase-based promoter assays

Promoter activity was assessed using the Dual-Glo Luciferase Assay System (Promega) according to the manufacturer's instructions. Briefly, LNCaP cells were seeded at ~50% confluency in 12-well plates (Corning Inc.) and transiently transfected with pGL3 Promoter Vector constructs containing wild-type androgen receptor (AR) binding sites using jetOPTIMUS (Polyplus Transfection). For androgen stimulation, cells were serum-starved for 24 h and subsequently treated with 10 nM DHT for 24 h in phenol red-free RPMI-1640 medium supplemented with 5% CSS. For androgen deprivation, cells were serum-starved for 24 h and treated with 20 µM Enza or Bica for 24 h. Similarly, DU145 cells were seeded at ~50% confluency and co-transfected with pGL3 promoter constructs containing wild-type (WT) or mutant (Mut) AR binding sites, or AR non-binding regions (NB), along with increasing concentrations of flag-tagged AR or ARΔDBD expression plasmids. At 48 h post-transfection, cells were

harvested, washed with 1× PBS, and lysed in 100 µL of 1× passive lysis buffer (PLB). Subsequently, 20 µL of lysate was mixed with 100 µL of luciferase assay reagent (LAR), and Firefly and Renilla luciferase activities were measured using the Synergy H1 Multimode Microplate Reader (BioTek Instruments), following a 5 sec delay and a 10 sec measurement window. Firefly luciferase activity was normalized to Renilla luciferase activity for each sample.

Generation of DUOX1 expressing stable cell lines

The DUOX1 cDNA (NCBI RefSeq: NM_017434.4) cloned into the pCMV3 vector was obtained from Sino Biological. The DUOX1 coding sequence was re-amplified and subcloned into the pLVX-TetOne-Puro (Takara Bio) at *Eco*RI and *Bam*HI restriction sites. For generation of stable cell lines, Lenti-X 293T cells were transfected with pLVX-TetOne-Puro-DUOX1 in the presence of pMDG and psPAX2 packaging plasmids using $CaPO_4$ transfection method. At 48 h post-transfection, lentivirus particles were collected and ~5×10^5 LNCaP or MyC-CaP cells were transduced in the presence of 8 µg/mL polybrene. The culture medium was replaced the following day, and puromycin selection was initiated 72 h post-transduction to establish the stable cell lines. Inducible expression of DUOX1 was validated by WB and qPCR analyses in the presence and absence of DOX.

Cell proliferation analysis

LNCaP wild-type and DUOX1-stably expressing LNCaP or MyC-CaP cells were seeded into each well of 12-well plates and either left untreated or treated with 1 µg/mL DOX for 3 days. Cell proliferation was assessed by determining viable cell numbers using the 0.4% trypan blue exclusion assay (Thermo Fisher Scientific) with an automated cell counter (Bio-Rad).

Cell cycle analysis

Cell cycle analysis was performed as previously described [37]. Briefly, LNCaP cells stably expressing DUOX1 were either left untreated or treated with 1 µg/ml DOX. After 48 h of treatment, cells were

washed with 1× PBS and fixed in ice-cold 70% ethanol (Merck Sigma-Aldrich) for 30 min at 4^0C, with ethanol added dropwise under continuous vortexing to prevent cell clumping. Cells were then washed twice with 1× PBS. Fixed cells were then treated with staining buffer containing 5 µg/ml propidium iodide (PI; Merck Sigma-Aldrich), 40 µg/ml RNase A (New England Biolabs), and 0.1% Triton X-100 in PBS for 30 min at room temperature. Samples were analyzed using the S3e Cell Sorter (Bio-Rad). Cell cycle distribution data were processed and analyzed using FCS Express v6.

Apoptosis assay

Apoptosis analysis was performed as previously described [37]. Briefly, LNCaP cells stably expressing DUOX1 were either left untreated or treated with 1 µg/ml DOX. After 48-72 h of treatment, cells were gently trypsinized, collected by centrifugation at 1800 rpm for 5 min, and resuspended in 500 µL of 1× annexin V binding buffer. Cells were stained with 5 µl each of FITC-conjugated annexin V (BioLegend) and PI for 5 min at room temperature in the dark. Annexin V binding and PI staining were analyzed using the S3e Cell Sorter (Bio-Rad), and data were processed using FCS Express v6. For fluorescence imaging, a subset of stained cells was further analyzed by microscopy. Nuclei were counterstained with Hoechst 33342 for 30 min at room temperature, followed by three washes with 1× PBS. Cells were mounted using antifade mounting medium. Images were acquired using the Zeiss AXIO Observer Z1 and analyzed with ZEN software (Carl Zeiss).

Wound healing assay

LNCaP cells stably expressing DUOX1 were either left untreated or treated with 1 µg/ml DOX. Cells were grown to confluence in 6-well plates, and a linear scratch (~2 mm) was created across the monolayer using a sterile pipette tip. Detached cells were gently removed by washing with 1× PBS. Wound closure was monitored over a period of 72 h using a phase-contrast microscope. Wound closure was quantified using ImageJ software by measuring the wound area at each time point relative

to the initial wound area at 0 h. The percentage of wound closure was used as a measure of cell migration.

Transwell migration assay

Cell migration was assessed using Transwell Boyden chambers with 6.5 mm diameter polycarbonate membrane inserts with 8 µm pore size (Corning). LNCaP cells stably expressing DUOX1 were either left untreated or treated with 1 µg/ml DOX to induce DUOX1 expression. After 48 h of treatment, cells were trypsinized, counted, and 1×10^5 cells were resuspended in serum-free RPMI-1640 medium and seeded into the upper chamber of the inserts. The lower chamber was filled with RPMI-1640 medium supplemented with 30% FBS as a chemoattractant. Following incubation for 48 h at 37^0C in a humidified incubator with 5% CO_2, non-migrated cells on the upper surface of the membrane were gently removed using a cotton swab. Migrated cells on the lower surface were fixed with 4% paraformaldehyde and stained with 0.5% (w/v) crystal violet. Representative images were captured using an Axio Observer Z1 microscope (Carl Zeiss). For quantitative analysis, stained cells were destained with 10% (v/v) acetic acid in distilled water, and absorbance was measured at 550 nm using a microplate reader.

Tumorsphere formation assay

Parental or DUOX1-overexpressing LNCaP cells were seeded at a density of ~3.5×10^4 cells per well in ultra-low attachment 6-well plates (Corning). Cells were cultured in serum-free DMEM/F12 (Gibco) media supplemented with 1x B27 (Invitrogen), 20 ng/ml epidermal growth factor (EGF; Invitrogen), 10 ng/ml fibroblast growth factor (FGF; Invitrogen), 2 mM L-glutamine (Invitrogen), and 100 U/ml penicillin-streptomycin (Gibco) at 37^0C in a humidified incubator with 5% CO_2. Primary tumorspheres were collected after the initial growth period, mechanically dissociated into single-cell suspensions by gentle pipetting, and reseeded in fresh sphere-forming medium under identical conditions to evaluate self-renewal capacity. As required, cells were subsequently treated with vehicle control (DMSO), Enza

or DOX by direct addition to the culture medium. After 10 days of culture, tumorspheres were quantified based on number and size using phase-contrast microscopy, and representative images were captured. For downstream analysis, tumorspheres were harvested and processed for total RNA isolation.

Detection of extracellular hydrogen peroxide (H_2O_2)

Extracellular H_2O_2 production was quantified using the Amplex Red Hydrogen Peroxide/Peroxidase Assay Kit (Thermo Fisher Scientific) according to the manufacturer's instructions. Parental or DUOX1-overexpressing LNCaP cells were either left untreated or treated with 1 µg/ml DOX to induce DUOX1 expression. After 48 h of treatment, cells were harvested and resuspended in Krebs-Ringer phosphate glucose (KRPG) buffer (145 mM NaCl, 5.7 mM sodium phosphate, 4.86 mM KCl, 0.54 mM $CaCl_2$, 1.22 mM $MgSO_4$, and 5.5 mM glucose; pH 7.35). For the assay, 1.5×10^4 cells in 20 µl KRPG buffer were added to 100 µl of reaction mixture containing 50 µM Amplex Red reagent (10-acetyl-3,7-dihydroxyphenoxazine) and 0.1 U/ml horseradish peroxidase (HRP) prepared in KRPG buffer, in pre-warmed black 96-well plates (Greiner Bio-One). In the presence of HRP, Amplex Red reacts with H_2O_2 in a 1:1 stoichiometry to generate the red-fluorescent product resorufin. Following incubation at room temperature for 30 min in the dark, fluorescence intensity was measured using a Synergy H1 multimode microplate reader (BioTek) with excitation at 550 nm and emission at 590 nm. Background fluorescence from no-H_2O_2 control reactions was subtracted from all readings.

Cell death reversal by N-Acetyl-L-cysteine (NAC)

Cell death and its reversal by the antioxidant NAC were assessed using fluorescent dyes Hoechst 33342, sulforhodamine B (SRB) and PI. LNCaP and MyC-CaP cells stably expressing DUOX1 were seeded at a density of 1.5×10^4 cells per well in 96-well plates (Corning). Cells were either left untreated or treated with 1 µg/ml DOX to induce DUOX1 expression, in the absence or presence of 5 mM NAC. 48 h post-treatment, cells were incubated with Hoechst 33342, SRB or PI according to

standard staining protocols. Fluorescence intensity was measured using a Synergy H1 multimode microplate reader (BioTek) at the following excitation/emission (Ex/Em) wavelengths - Hoechst 33342 (350/461 nm), SRB (565/586 nm), and PI (535/617 nm). Relative fluorescence units (RFU) were used to assess changes in cell viability and cell death, and the extent of NAC-mediated rescue was calculated relative to DOX-treated samples.

RNA sequencing and data analysis

LNCaP cells stably expressing DUOX1 were either left untreated or treated with 1 µg/ml DOX for 48 h prior to RNA isolation. Total RNA was extracted using the RNeasy Mini Kit (Qiagen) according to the manufacturer's instructions, and RNA quality and integrity were assessed by gel electrophoresis prior to library preparation. ~1 µg of total RNA per sample was used for library construction using the NEBNext Ultra II Directional RNA Library Prep Kit (New England Biolabs), following the manufacturer's instructions. Libraries were sequenced on an Illumina NovaSeq 6000 platform to generate high-throughput paired-end reads. Raw sequencing reads were subjected to quality assessment using FastQC. Adapter sequences and low-quality bases were trimmed using Trimmomatic (v0.35). The processed reads were aligned to the human reference genome (Homo sapiens, GRCh37) using Bowtie2 (v2.7.12) with default parameters. Gene-level read counts were obtained using featureCounts (v2.0.3). Differential gene expression analysis was performed using the limma-voom (v3.58.1) package in R. Genes with a $\log_2$ fold change ≥ 1 or ≤ -1 and a P-value ≤ 0.001 were considered significantly differentially expressed. Functional enrichment analysis of differentially expressed genes was carried out using the DAVID v6.8 web server. Gene Ontology (GO) terms were extracted from the annotation clusters to identify significantly enriched biological processes and pathways. All analyses were performed using default parameters unless otherwise specified. Raw RNA-Seq data along with the corresponding downstream analyses are presented in Dataset S2.

Dihydrotestosterone (DHT) ELISA

Extracellular DHT levels in conditioned media were quantified using a competitive DHT ELISA kit (FineTest) according to the manufacturer's instructions. LNCaP cells stably expressing DUOX1 were cultured in RPMI-1640 medium supplemented with either regular FBS or CSS. Cells were subsequently treated with 1 µg/ml DOX to induce DUOX1 expression. 48 h post-treatment, culture supernatants were collected by centrifugation at 2500 rpm for 5 min at 4^0C. A total of 20 µL of each supernatant was used for the ELISA assay. DHT levels were measured at 450 nm using a microplate reader, following the competitive ELISA protocol. DHT concentrations were calculated based on a standard curve generated using known concentrations of DHT provided in the kit.

Statistical analysis

Unless otherwise specified, data are presented as mean ± standard deviation (SD) from at least three independent biological replicates (n ≥ 3). Statistical analyses were performed using GraphPad Prism (v8) or Microsoft Excel (2021). For comparisons between two groups, unpaired two-tailed Student's t-test or Welch's t-test (for unequal variances) was applied as appropriate. For comparisons involving more than two groups, ordinary one-way ANOVA followed by Sidak's or Tukey's multiple comparisons test, or two-way ANOVA where applicable, was used. In cases where data did not meet parametric assumptions, the non-parametric Kruskal-Wallis test was employed. A p-value < 0.05 was considered statistically significant. Statistical significance is denoted as follows - $p < 0.05$ (*), $p < 0.01$ (**), $p < 0.001$ (***), and not significant (ns).

Results

DUOX1 is a methylation-driven potential biomarker for prostate cancer

Several biased and unbiased genome-wide methylation studies have previously reported promoter hypermethylation of TSGs in PCa [13-19]. To identify methylation-driven genes associated with PCa risk in a more stringent manner within an Indian population, we performed global DNA methylation profiling using the Infinium MethylationEPIC 850K BeadChip array on a prospective 'discovery cohort' comprising 8 benign prostatic hyperplasia (BPH) and 8 PCa tissue biopsy specimens (Figure 1A). Among the 1,51,730 promoter-embedded CpG sites corresponding to 22,255 genes, probes exhibiting ≥20% difference in β-value between PCa and BPH were considered for further analysis (Figure 1A-B). This filtering yielded 23 differentially methylated genes with statistical significance determined by FDR-adjusted $p < 0.05$ (Figure 1A, C).

Cross-comparison with TCGA prostate adenocarcinoma (PRAD) datasets for promoter methylation (SMART, UALCAN) and gene expression (GEPIA2, UALCAN) refined the candidate list to 11 hypermethylated genes (Figure 1A, D). Among these, DUOX1 exhibited one of the most significant with highest degrees of promoter hypermethylation in PCa relative to BPH (Figure 1D, E). Consistent with its promoter hypermethylation, qPCR analysis of RNA isolated from an independent 'validation cohort' containing 8 BPH and 8 PCa tissue biopsy specimens revealed significant downregulation of DUOX1 transcripts in PCa samples compared to BPH (Figure 1F).

DUOX1's role in cancer is complex and context-dependent, acting as a tumor suppressor in some settings by inhibiting cell growth and promoting cell cycle arrest [28,30], while in others contributing to tumor progression [32,33]. However, to date, its precise role in PCa pathogenesis remains largely unclear. TCGA analysis demonstrated DUOX1 expression was significantly downregulated in most of the solid cancers including PCa (Figures S1A and 1G). Consistent with our 850K methyl array results, reanalysis of 450K methyl array data from the TCGA PRAD cohort and two publicly available datasets of normal and metastatic prostate tissues demonstrated significant promoter methylation of DUOX1 gene (Figures 1H and Figure S2A-B). Pearson correlation analysis of

TCGA PRAD data revealed a strong negative association between DUOX1 promoter methylation and its expression (Figure 1I), which was further evident with increasing age in PCa patients' samples (Figure S1B-C). Despite substantial inter- and intraobserver variability, the Gleason score remains one of the most important tissue-based prognostic markers for PCa patients [38,39]. DUOX1 expression was significantly downregulated with increasing Gleason score 6-10 in TCGA PRAD samples (Figure S1D), indicating that DUOX1 expression could be utilized as a prognostic biomarker for PCa patients. DUOX1 functions as a protein complex co-assembled from the catalytic DUOX1 and the auxiliary DUOXA1 subunits [40]. DUOX1 and DUOXA1 genes are located on chromosome 15q15-21 in a complex, bidirectionally arranged locus (Figure S3A). Pearson correlation analyses demonstrated that DUOX1 and DUOXA1 expressions were tightly linked ($r = 0.951$, $p < 0.0001$) in TCGA PRAD samples (Figure S3B). Moreover, similar to DUOX1, DUOXA1 expression was similarly regulated by promoter-methylation in TCGA PRAD cohort (Figure S3C-E).

While overall survival (OS) remains the gold standard, composite outcomes such as progression-free survival (PFS) and disease-free survival (DFS) are increasingly used as surrogate primary endpoints in cancer research and clinical trials [41]. In advanced stages of PCa patients, such as mCRPC, PFS is frequently utilized as a primary endpoint due to challenges in accurately evaluating OS [42]. Kaplan-Meier analysis demonstrated that TCGA PRAD patients' cohort with elevated DUOX1 expression was associated with better PFS and disease-free survival (DFS) (Figures 1J and S1E). However, there was no significant correlation of DUOX1 expression with OS of PCa patients (Figure S1F). Overall, the data indicate that the methylation status of the DUOX1 gene could be a suitable indicator of PCa development.

Inhibition of DNA-methylation enhances DUOX1 expression and cell death in androgen-sensitive PCa cells

The concordance of elevated promoter hypermethylation and reduced expression in independent patients' cohorts suggest that DUOX1 may function as a methylation-driven TSG in PCa,

591 warranting further mechanistic investigation in cell line model. To this end, we first checked DUOX1
592 expressions in different prostate cell lines (n=12) using DepMap portal. Based on differential DUOX1
593 expression levels, we chose two cell lines – androgen-sensitive LNCaP and androgen-refractory DU145
594 cells. DU145 represents CRPC model with very low or undetectable AR expression [43]. DepMap cell
595 line analysis revealed that DUOX1 expression was markedly downregulated in AR-positive LNCaP cells
596 as compared to AR-negative DU145 cells (Table S4). Both WB and qPCR analysis further validated
597 differential DUOX1 expressions in LNCaP and DU145 cells (Figure 2A-B). Next, to determine whether
598 promoter methylation can regulate DUOX1 expression in these two cell lines, we first reanalysed 450K
599 methyl array data. The results demonstrated that poorer DUOX1 expression was due to greater
600 promoter methylation in LNCaP cells as compared to DU145 cells (Figure 2C). To corroborate this
601 notion, LNCaP and DU145 cells were treated with 4 μM decitabine (5-aza-2'-deoxycytidine; Aza), a
602 hypomethylating agent, for 48 h and subjected to qPCR and WB analysis (Figure 2D-E). In contrast to
603 DU145 cells, Aza treatment resulted in an increased DUOX1 expression in AR-positive LNCaP cells at
604 both transcriptional and translational levels (Figure 2D-E). Reanalysis of microarray data of Aza treated
605 multiple PCa lines – LNCaP, DU145 and 22Rv1 further confirmed that DUOX1 expression is indeed
606 controlled by promoter hypermethylation (Figures 2F and S4A-C). However, there was no significant
607 change in promoter methylation pattern of AR gene among LNCaP and DU145 cells or AR expression
608 at least at the transcription level in post-Aza treated various PCa lines (Figure S4A-E).
609 Previous studies suggest that Aza treatment can induce cell death in both AR-positive and AR-
610 negative PCa cells [43]. It has been proposed that Aza can be utilized in treatment regimen in patients
611 with hormone-refractory and chemoresistant PCa [44, 45]. Aza-mediated elevated DUOX1 expression
612 prompted us to examine cell death in these two PCa cell lines. As compared to DU145, LNCaP cells
613 were significantly more sensitive to Aza-mediated cell death (Figure 2G-H). Aza treatment further
614 demonstrated decreased colony formation ability and increased intracellular ROS generation in AR-
615 sensitive LNCaP cells (Figure 2I-J).
616

De novo DNA methyltransferase enzymes are responsible for DUOX1 promoter hyeprmethylation

DNA methyltransferase (DNMT) enzymes transfer methyl group from S-adenosyl-L-methionine to the 5'-position of cytosine residues in DNA. There are four members in the DNMT family, which includes DNMT1, DNMT3A, DNMT3B and DNMT3L. Although not fully understood, DNMT1 is generally considered to be involved in maintenance DNA methylation, whereas DNMT3A and DNMT3B primarily mediate *de novo* DNA methylation. DNMT3L, a DNMT3-like protein lacking a catalytic domain, promotes DNMT3A and DNMT3B mediated de novo DNA-methylation [46,47]. Considering their strong involvement in the development of various cancers including PCa [47,48], we first checked the expression of all three major DNMTs among various prostate epithelial cell lines in DepMap portal as well as in TCGA PRAD patients' samples (Figure 2K-L). DepMap data of six prostate adenocarcinoma cell lines (PC3, DU145, LNCaP, VCaP, MDAPCa2B and 22Rv1) demonstrated that DUOX1 expression was negatively correlated with both DNMT1 and DNMT3A but not with DNMT3B (Figure 2K and Table S4). In TCGA PRAD samples, DNMT1 and DNMT3A transcripts were markedly more abundant than DNMT3B; however, DNMT3A and to a lesser extent, DNMT3B, were significantly upregulated in the malignant cohort (n = 497) relative to normal samples (n = 52), while DNMT1 remained unchanged (Figure 2L). WB and qPCR analysis of all three DNMTs revealed that in contrast to DU145, LNCaP cells had significantly higher DNMT3A and DNMT3B expressions at both protein and transcript levels (Figure 2M-N). Aza treatment significantly declined all three DNMT protein levels in LNCaP cells (Figure 2O). Reanalyses of RNA-Seq data of decitabine/Aza-treated C4-2B, a castration-resistant sub-line derived from LNCaP cells [49], revealed significant upregulation of DUOX1 transcript without affecting RNA levels of both DNMT3A and DNMT3B (Figure S4F). A similar phenomenon was also observed in qPCR analysis of Aza treated LNCaP cell (Figure S4G), indicating that Aza deregulates both *de novo* DNMTs by acting on their protein levels. This led us to hypothesize that increased DNMT3A and DNMT3B expressions at protein level might negatively regulate DUOX1 transcription in LNCaP cells.

Next, we sought to determine whether DNMT3A or DNMT3B is directly involved in regulating DUOX1 expression in PCa cells. Given that DNMT3A is expressed at higher levels than DNMT3B in LNCaP cells, we first performed shRNA-mediated knockdown of DNMT3A (Figure 2P). DNMT3A depletion resulted in a substantial increase in DUOX1 expression in LNCaP cells (Figure 2P). Interestingly, DNMT3A knockdown also led to a significant upregulation of DNMT1, possibly reflecting a compensatory response (Figure 2P). To further corroborate these findings, we utilized a non-nucleoside inhibitor, DY-46-2, which specifically targets DNMT3A activity [50] (Figure 2Q). Consistent with DNMT3A knockdown, DY-46-2 treatment markedly increased DUOX1 expression and induced cell death (Figure 2Q-R). To further validate, LNCaP cells were transiently transfected with either DNMT3A or DNMT3B expression vectors and subjected to WB analysis (Figure S5A-B). Ectopic expression of both DNMT3A and DNMT3B resulted in reduced DUOX1 expression (Figure S5A-B).

Our 850K methyl array consists of total 15 CpG probes in the DUOX1 promoter region within 1.39 Kb from the transcription start site (TSS) (Figure 2S). To further confirm the DNA-methylation pattern within DUOX1 promoter, we reanalysed 5-mC ChIP-Seq data in LNCaP cells (Figure 2T). The results demonstrated a strong 5-mC peak at the DUOX1 promoter region (Figure 2T). Reanalysis of genome-wide bisulfite sequencing of LNCaP and DU145 cells demonstrated that DUOX1 promoter region was profoundly methylated in LNCaP cell as compared to DU145 (Figure 2U). To validate whether DNMT3A or DNMT3B is associated with the methylation of this region, we designed two ChIP-qPCR primer sets (Figure 2V-X). ChIP-qPCR analysis using specific antibodies against all three DNMT members demonstrated that DNMT3A and to a lesser extent DNMT3B were significantly recruited onto the DUOX1 promoter region in LNCaP but not in DU145 cells (Figure 2V-X). Overall, our results established that DUOX1 is a methylation driven TSG, whose expression, at least in part, is controlled by DNMT3A and DNMT3B mediated promoter hypermethylation.

AR suppresses DUOX1 expression in PCa samples and cell line models

AR is a critical driver of normal prostate growth as well as PCa development [51-54]. AR can function as both a transcriptional activator and a repressor, thereby impacting PCa development [55-57]. Depleted DUOX1 expression in AR-positive LNCaP cells prompted us to examine a potential link between DUOX1 and AR expression in PCa patients. Hierarchical clustering of top 150 RNA-Seq datasets of TCGA-PRAD cohort demonstrated that DUOX1 expression was negatively correlated with AR (Figure 3A). Next, we stratified prostate epithelial cell lines (n=12) available at DepMap portal based on high and low AR expression levels (Figure 3B and Table S4). The cells with higher AR expression exhibited a significantly lower expression of DUOX1 and contrariwise (Figure 3B). A similar trend was also detected for DUOXA1 in both TCGA PRAD and DepMap samples (Figure S6A-B). Likewise, another independent clinical RNA-Seq dataset demonstrated a decreased expression of DUOX1 and DUOXA1 transcripts in more advanced stage aggressive PCa as compared to BPH samples (Figure S6C). Since TCGA-PRAD data are derived from bulk RNA-Seq, the observed inverse correlation may be confounded by tumor heterogeneity. To address this, we analyzed single-cell RNA-Seq (scRNA-Seq) data from prostate tumor samples (Figure S7). In both low- and high-grade PCa tissues, DUOX1 expression was enriched in normal prostate epithelial cells but markedly reduced in tumor epithelial cells, whereas AR expression showed the opposite pattern (Figure S7). Taken together, our results established a robust inverse correlation between AR and DUOX1 expression during PCa progression.

To further validate this association, LNCaP cells were knockout (KO) for AR using two specific sets of sgRNAs (Figure 3C). The efficiency of KO was validated by WB analysis (Figure 3C). Intriguingly, KO of AR markedly enhanced DUOX1 expression (Figure 3C). In contrast, ectopic expression of GFP-tagged AR expressing construct in AR-negative DU145 cells significantly declined endogenous DUOX1 expression at both protein and transcript levels (Figure 3D-E). Reanalysis of RNA-Seq data of siRNA-mediated AR knockdown (KD) in LNCaP, VCaP and 22Rv1 cells showed analogous increased DUOX1 transcript (Figure 3F). Likewise, reanalysis of RNA-Seq data of hormone stimulated VCaP cells with androgen analogue, R1881, displayed decreased DUOX1 expression, while AR inhibitor, enzalutamide (Enza), treatment significantly enhanced DUOX1 expression (Figure 3G). Although pharmacological

693 inhibitors for AR - Enza and bicalutamide (Bica) have been extensively used for the treatment of both
694 locally advanced non-metastatic and metastatic subgroups, Enza demonstrated significantly better
695 outcomes in patients with mCRPC [58,59]. In agreement to this, Enza and Bica treatment in LNCaP
696 cells substantially increased DUOX1 expression at both protein and RNA levels (Figure 3H-I). As
697 expected, Enza and Bica treatment also significantly enhanced intracellular ROS levels in LNCaP cells
698 (Figure 3J). Enhanced DUOX1 expression in LNCaP cells in response to anti-androgen treatment was
699 further validated using IF analysis (Figure 3K). Taken together, our findings demonstrated that AR
700 signalling negatively regulates DUOX1 expression and draws attention to AR antagonists mediated
701 upregulation of DUOX1 in PCa.
702
703 **AR represses DUOX1 expression via direct binding to its regulatory region**
704 AR regulates gene expression through binding to androgen-response elements (AREs) located
705 within the promoter and enhancer regions of target genes [56,57]. To examine whether AR directly
706 regulates DUOX1 transcription we reanalysed AR ChIP-Seq data in LNCaP and VCaP cells (Figures 4A
707 and S8A). ChIP-Seq analysis confirmed specific AR recruitment onto an intragenic enhancer region of
708 DUOX1 gene (Figures 4A and S8A). We further examined AR recruitment on DUOX1 gene in another
709 dataset comprising normal prostate and PCa tissue samples (Figure S8B). As compared to the normal
710 counterpart, a significant AR enrichment was observed onto the putative enhancer element of DUOX1
711 in PCa cohort (Figure S8B). To determine the presence of AR binding sites in this enhancer region, we
712 scanned for the presence of AREs in the ~10 kb downstream of transcription start site (TSS) comprising
713 of the entire DUOX1 gene using JASPAR software [60]. One single *p*-value corrected ($p<0.05$) putative
714 ARE (AGGAACAATCTGTGC) was identified within the corresponding ChIP-Seq signal of positive DNA
715 strand (Figure 4B-C). Next, to confirm AR binding on the DUOX1 enhancer region, we performed ChIP-
716 qPCR for AR in androgen stimulated LNCaP cells (Figure 4D). To this end, we designed ChIP-qPCR
717 primers for one AR non-binding region (NB site) close to the DUOX1 promoter as a negative control
718 and two overlapping AR-binding regions (sets 1 and 2) containing the putative ARE (Figure 4B). Upon

androgen stimulation, a significant enrichment for AR-binding using both primer sets was observed, while no binding was observed in the NB region of DUOX1 gene in androgen stimulated LNCaP cells (Figure 4D). Specific primer set for AR binding region on KLK2 promoter [61] was used as positive control in ChIP-qPCR analysis (Figure 4D).

Upon androgen stimulation, specific AR recruitment onto DUOX1 enhancer region, further prompted us to examine AR signalling-mediated transcriptional repression of DUOX1 (Figure 4E). To this end, we amplified the AR-binding region containing ARE and subsequently cloned into pGL3-promoter vector and subjected to luciferase reporter assay in LNCaP cells (Figure 4F). While androgen stimulation resulted in a sharp reduction in the luciferase activity, a significant increase in the luciferase activity was observed upon anti-androgen treatment with either Enza or Bica (Figure 4F).

FOXA1 is a pioneer factor for AR-regulated enhancer [56]. Moreover, FOXA1 recruits LSD1-CoREST complex at the AR regulated enhancers and suppresses basal transcription of the AR target genes through H3K4 demethylation [62]. Reanalysis of ChIP-seq data of DU145 cells stably expressing a ligand-binding AR mutant (Q640X), which is unable to interact with FOXA1, showed similar enrichment at the DUOX1 locus overlapping that of wild-type (WT) AR. In contrast, AR mutants C562S and G568W, which lack DNA-binding ability but retain the capacity to interact with FOXA1, showed no binding at the DUOX1 enhancer region (Figure 4G). Reanalysis of ChIP-Seq data in VCaP cells, together with ChIP-qPCR validation in LNCaP cells, demonstrated that FOXA1 recruitment to the DUOX1 regulatory region is dependent on AR occupancy in androgen-stimulated PCa cells (Figure S9A-B). In contrast, no variance in AR occupancy profiles onto DUOX1 regulatory region was observed upon FOXA1 knockdown in androgen stimulated LNCaP cells (Figure S9C). Moreover, reanalysis of RNA-Seq of FOXA1 KD in LNCaP and VCaP cells showed no change in DUOX1 expression (Figure S9D-E). Consistently, FOXA1 overexpression or KO in LNCaP cells failed to modulate DUOX1 expression (Figure S9F-G). Collectively, these findings indicate that FOXA1 is dispensable for DUOX1 regulation, while AR DNA-binding activity is critical for controlling DUOX1 transcription.

744 To further validate AR direct recruitment and transcriptional suppression of DUOX1, we
745 performed luciferase reporter assay in DU145 cells transiently transfected with three different DUOX1
746 enhancer constructs containing WT ARE, mutant ARE and AR non-binding (NB) site in the presence of
747 increasing concentrations of flag-tagged AR (Figure 4H, I). A dose-dependent decrease in luciferase
748 activity was observed in cells transfected with the WT ARE construct, whereas no significant change
749 was detected with either the mutant ARE or AR non-binding constructs (Figure 4I). To further assess
750 the requirement of AR DNA-binding activity in DUOX1 repression, we generated a flag-tagged AR
751 construct lacking the DNA-binding domain (ΔDBD; residues 559–664) (Figure 4J). Luciferase-reporter
752 assays revealed that, in contrast to WT AR, the ΔDBD mutant failed to suppress the activity of the WT
753 ARE reporter construct in DU145 cells (Figure 4K). Collectively, these findings demonstrate that the
754 DNA-binding ability of AR is essential for its recruitment to the DUOX1 regulatory region and the
755 subsequent transcriptional repression of DUOX1.
756
757 **AR-associated H3K27ac-BRD4 complex forms a negative loop to suppress DUOX1 expression**
758 To delineate the transcriptional network governing AR occupancy at the DUOX1 regulatory
759 region, we reanalysed publicly available ChIP-Seq datasets for PCa-specific TFs, chromatin modifiers,
760 and histone marks across multiple AR-positive PCa cell lines (Figure 5A). Reanalysis of ATAC-Seq data
761 in DHT-treated LNCaP cells demonstrated increased chromatin accessibility at the AR binding region
762 (Figure 5A), suggesting that DUOX1 transcription may be regulated via androgen-induced recruitment
763 of specific TFs and histone modifications at the DUOX1 intragenic AR binding region. ChIP-Seq profile
764 further revealed that the AR binding region coincided with RNA polymerase II (RNA-Pol II) and the
765 epigenetic reader BRD4 peaks upon androgen stimulation in AR positive LNCaP and 22Rv1 cells (Figure
766 5A). Additional ChIP-Seq datasets confirmed that pharmacological inhibition of AR in VCaP cells or
767 siRNA-mediated AR knockdown in 22Rv1 cells markedly reduced RNA-Pol II recruitment at the AR
768 binding region (Figure S10A), indicating that AR engages an active enhancer complex to mediate
769 DUOX1 transcriptional suppression.

BRD4, a member of the bromodomain and extraterminal domain (BET) family, associates with chromatin through recognition of acetylated histones, acting as a 'reader' that recruits transcriptional machinery to regulate gene expression [63-65]. Among these modifications, BRD4 is closely linked to H3K27ac, a hallmark of active enhancers, and is essential for maintaining enhancer activity [66-68]. Moreover, BRD4 directly interacts with AR and is critical for sustaining AR-driven transcriptional programs [69]. Given that H3K27ac-enriched enhancers serve as key chromatin sites for BRD4 recruitment [68], we hypothesized that H3K27ac-mediated recruitment of BRD4 to the DUOX1 enhancer facilitates AR-dependent transcriptional reprogramming. Consistent with this hypothesis, ChIP-Seq analysis in LNCaP cells revealed strong H3K27ac signals at the AR enhancer region even in the absence of androgen stimulation (Figure 5A), suggesting a pre-established chromatin landscape conducive to BRD4 binding. ChIP-qPCR assays further validated androgen stimulation induced both H3K27ac and BRD4 enrichment at the AR binding site in LNCaP cells (Figure 5B-C).

Pharmacological inhibition of BRD4 is known to disrupt AR binding to AREs [69]. Small-molecule BET inhibitors (BETis), such as JQ1, competitively displace BET proteins from acetylated lysines on histones and TFs, thereby attenuating oncogenic transcription and reducing cancer cell viability [70,71]. Indeed, BETis have emerged as promising therapeutic agents, particularly in advanced PCa and CRPC [71-73]. Consistent with this, JQ1 treatment in LNCaP cells significantly upregulated DUOX1 expression at both protein and transcript levels (Figure 5D-E) and concomitantly reduced cell viability (Figure 5F). Similar to AR inhibition, JQ1 treatment markedly decreased RNA-Pol II occupancy at the AR binding site (Figure S10A), likely disrupting the AR transcriptional complex to relieve DUOX1 repression. In contrast to DUOX1, several oncogenes are transcriptionally activated by BRD4 [73,74]. For instance, BRD4 enhances MYC expression to promote PCa cell proliferation [73,74]. Reanalysis of RNA-Seq data revealed that BRD4 depletion via siRNA elevated DUOX1 expression, while AR and MYC transcripts were concurrently suppressed (Figure 5G). To further confirm BRD4's role, LNCaP cells were subjected to BRD4 KO using two sets of sgRNAs (Figure 5H). WB analysis verified that only sgRNA set #2 effectively ablated BRD4 expression, which correspondingly led to a marked increase in DUOX1

protein levels compared with control and non-functional sgRNA set #1 (Figure 5H). Consistent with its functional significance, BRD4 expression is significantly elevated in PCa [76]. Reanalysis of TCGA-PRAD patient sample and DepMap PCa cell line datasets revealed a strong negative correlation between BRD4 and DUOX1 expression (Figure S10B-C).

H3K27ac plays a crucial role in PCa pathogenesis, with a substantial proportion of PCa heritability localized within H3K27ac-marked genomic regions [76]. Intriguingly, reanalysis of H3K27ac ChIP-Seq datasets from normal prostate tissue, primary PCa, and CRPC samples revealed a redistribution of H3K27ac peaks, from the DUOX1 promoter region in normal prostate to the intragenic AR binding region in both PCa and CRPC samples (Figure 5I). A similar pattern of H3K27ac peak redistribution was also observed in PCa cell lines (LNCaP and VCaP) compared with normal primary prostate epithelial cells (PrEC) and the non-tumorigenic, immortalized prostate epithelial line RWPE-1 (Figure S10D). While independent treatment with Aza or Enza enhanced DUOX1 expression, combined treatment with Aza and Enza did not further increase DUOX1 levels and cell death beyond those observed with individual treatments (Figure 5J-K). Moreover, Enza-mediated restoration of DUOX1 expression occurred through specific downregulation of AR, thereby reducing its recruitment to the DUOX1 regulatory region (Figure 5J). The shift in enhancer-associated acetylation reflects a reprogramming of chromatin activity during PCa progression, favouring H3K27ac-BRD4-AR driven transcriptional networks over DUOX1 expression (Figure 5L). Together, these findings indicate that the H3K27ac-BRD4-AR axis establishes a repressive circuit on DUOX1, and restoration of DUOX1 expression may disrupt AR-dependent transcriptional programs and inhibit PCa cell proliferation.

Restoration of DUOX1 expression elicits antitumor effects through ROS-induced apoptosis and AR suppression

Given that DUOX1 expression is transcriptionally repressed by the H3K27ac-BRD4-AR axis, we next examined the functional impact of DUOX1 restoration in PCa. To this end, DUOX1 cDNA was cloned into a doxycycline (DOX)-inducible lentiviral vector and stably expressed in two AR-positive PCa

822 cell lines, LNCaP and Myc-CaP (Figures 6A and S11A). The Myc-CaP cell line was originally derived from
823 a prostate tumor in a transgenic mouse that had not undergone hormone ablation [77]. Upon DOX
824 induction for 48 h, DUOX1 expression was robustly upregulated in both cell lines, as confirmed by WB
825 and qPCR analyses (Figures 6B-C and S11B-C).

826 Steady DUOX1 expression markedly reduced cell proliferation, viability and colony formation
827 ability (Figure 6D-F and S11D-F). DOX treatment alone had no detectable effect on cell proliferation
828 or viability of parental LNCaP cells, confirming the specificity of the inducible system (Figure S12A-B).
829 Cell cycle analysis using PI staining revealed that DUOX1 induction led to an accumulation of LNCaP
830 cells in the sub-G1 phase (Figure 6G), suggesting apoptotic DNA fragmentation and hypodiploid
831 content. Consistently, microscopy and flow cytometry analysis of annexin V/PI dual staining further
832 confirmed enhanced apoptosis following DUOX1 restoration (Figures 6H and S13). During intrinsic
833 apoptosis the executioner caspases – caspase 3 (Casp3) and caspase 7 are activated by caspase 9
834 (Casp9) mediated cleavage, which in turn cleave PARP1 producing 89 kDa and 24 kDa fragments that
835 serve as hallmark of programmed cell death [78,79]. Apoptotic induction was additionally validated
836 by cleavage of Casp9, Casp3 and PARP1 in DUOX1-expressing LNCaP and Myc-CaP cells (Figures 6I
837 S11G). Studies suggest that enhanced DUOX1 activity in primary fibroblasts elevates ROS levels,
838 leading to increased early apoptotic markers such as cyclin-dependent kinase (CDK) inhibitor p21
839 expression, thereby negatively affecting wound healing [80]. Transcriptional activation of p53/TP53
840 and its downstream effector p21/CDKN1A in LNCaP-DUOX1 cells (Figure 6J) provided additional
841 mechanistic evidence linking DUOX1-mediated ROS production to apoptotic signalling.

842 Previous studies suggest that DUOX1 depletion promotes EMT in lung adenocarcinoma cells
843 [30]. In agreement, ectopic DUOX1 expression in LNCaP cells suppressed mesenchymal characteristics,
844 as indicated by weakened cell migration (Figure 6K-L). DUOX1-mediated reduction in cell migratory
845 ability was assessed using scratch wound healing (Figure 6K) and transwell migration assays (Figure
846 6L). In addition, compared to control cells, restoration of DUOX1 expression in both LNCaP and Myc-
847 CaP cells led to a marked loss of mesenchymal markers - β-catenin (β-Cat), vimentin (Vim), and Snail1,

accompanied by a significant upregulation of the epithelial marker desmoplakin (DSP) (Figures 6M S11H). These findings suggest that DUOX1 restoration inhibits EMT and may therefore limit PCa metastatic progression.

Low-to-moderate ROS levels generally promote EMT, whereas excessive ROS can inhibit EMT and trigger apoptosis [81]. As DUOX enzymes are major sources of extracellular H_2O_2 generation [82], we next assessed both intracellular and extracellular ROS in LNCaP-DUOX1 cells (Figure 6N-0). DOX-induced DUOX1 expression markedly increased total intracellular ROS and extracellular H_2O_2 (Figure 6N-O), while only DOX treatment alone had no effect on parental LNCaP cells (Figure S12C-D). Because NOX family enzymes and the mitochondrial electron transport chain are interlinked ROS sources [84], we examined mitochondrial superoxide levels using MitoSOX and observed a significant increase following DUOX1 induction (Figure S14), suggesting a feed-forward amplification of ROS production.

The relationship between ROS and AR expression in PCa is context-dependent. While mild to moderate ROS levels enhance AR signalling, excessive ROS suppresses AR transcription and translation [84-87]. We hypothesized DUOX1-induced ROS accumulation could modulate AR expression and its oncogenic activity (Figure 6P). Indeed, DOX-induced restoration of DUOX1 expression in LNCaP cells markedly reduced AR expression at both protein and transcript levels (Figure S15A-C). In contrast, DOX treatment alone had no effect on AR expression in parental LNCaP cells (Figure S15D-F). Increasing concentrations of extracellular H_2O_2 significantly downregulated AR expression in a dose-dependent manner (Figure S15G), suggesting DUOX1-mediated H_2O_2 production may influence AR expression. To determine whether the downregulation of AR expression was indeed a consequence of DUOX1-mediated ROS accumulation, LNCaP-DUOX1 stable cells were pre-treated with the antioxidant N-acetylcysteine (NAC) prior to DOX mediated DUOX1 expression (Figure 6Q). NAC administration markedly reversed DUOX1-induced apoptotic signalling, as evidenced by the disappearance of cleaved Casp3 and PARP1 bands in WB analysis (Figure 6Q), confirming the ROS dependency of DUOX1-mediated apoptosis.

Superoxide dismutase 2 (SOD2) is an antioxidant enzyme that catalyzes the dismutation of superoxide radicals ($O_2^{\bullet-}$) into H_2O_2 and molecular oxygen (O_2). The resulting H_2O_2 is subsequently decomposed by catalase (CAT), another key antioxidant enzyme, into water (H_2O) and O_2 [88,89]. However, neither DUOX1 restoration nor NAC pre-treatment had any effect on SOD2 or CAT expression (Figure 6Q). Glutathione peroxidase 4 (GPX4) serves as a crucial regulator of lipid peroxidation and ferroptosis [90]. Notably, DUOX1 has recently been shown to inhibit GPX4 in laryngeal squamous cell carcinoma cells [91]. Consistent with this, DUOX1 overexpression in LNCaP cells markedly reduced GPX4 expression, which was reversed upon NAC pre-treatment (Figure 6Q). DUOX1-induced, ROS-mediated apoptotic induction and its reversal by NAC treatment prompted us to further examine whether NAC could also rescue cell viability. Consistently, NAC pre-treatment significantly rescued DUOX1-induced loss of cell viability and clonogenic capacity of LNCaP and MyC-CaP cells (Figures 6R-U and S11I-J). To corroborate DUOX1-induced ROS-dependent cell death and its reversal by NAC, cell viability was assessed using three complementary approaches - Hoechst 33342 staining for viable nuclei (Figure 6R), SRB assay to quantify total protein content independent of metabolism (Figures 6S and S11I), and PI staining to identify dead or dying cells with compromised membranes (Figure 6T).

AR signalling and PCa stemness exhibit an inverse relationship, as loss of AR expression is associated with enhanced stem-like features and therapy resistance [92,93]. To determine whether DUOX1-mediated AR depletion could influence PCa stemness, we examined the expression of cancer stem cell (CSC) markers using the sphere formation assay in DUOX1 stably expressing LNCaP cells. qPCR analysis revealed DUOX1 overexpression following DOX treatment significantly increased the expression of SOX2, KLF4, and NANOG (Figure S16A-B). Consistent with previous reports [93], Enza treatment also transcriptionally activated the same set of CSC markers (Figure S16C-D). Collectively, these findings indicate that while DUOX1 restoration exerts potent antitumor effects through ROS-dependent apoptosis, AR suppression and EMT reversal, DUOX1-mediated AR depletion may concurrently enhance CSC properties.

DUOX1-driven transcriptomic rewiring impairs glucuronidation pathway in PCa

Hitherto, our findings support a model in which the H3K27ac-associated BRD4-AR complex represses DUOX1 expression to sustain AR-dependent oncogenic signalling, whereas restoration of DUOX1 counteracts this axis by suppressing AR activity and its metastatic potential. To delineate the DUOX1-mediated ROS-driven transcriptional network underlying PCa pathogenesis, we performed RNA-Seq analysis of LNCaP cells with or without DUOX1 induction following 48 h of DOX treatment (Figure 7A-B). Consistent with previous observations, global transcriptomic profiling also revealed a marked downregulation of AR expression upon DUOX1 re-expression (Figure 7A). Gene Ontology (GO) enrichment analysis further identified cellular glucuronidation (GO:0052695, p = 0.0000396) as the most significantly downregulated biological process in response to DUOX1 restoration (Figure 7C), suggesting that DUOX1-driven redox signalling may reprogram metabolic and detoxification pathways critical for PCa progression.

Given that glucuronidation plays a central role in androgen metabolism and clearance [94], we next explored whether DUOX1-mediated suppression of glucuronidation pathways could influence androgen signalling dynamics in PCa. Transcriptomic profiling revealed significant downregulation of multiple UDP-glucuronosyltransferase (UGT) family members, including UGT2B-7, -15, -17, -11 and -28 following DUOX1 induction (Figure 7D). UGT2B-7, -15 and -17 catalyse the glucuronidation of DHT and other steroidal metabolites, thereby modulating intracellular androgen availability and protect the androgen-sensitive tissues from deleteriously elevated hormone concentrations [95]. In contrast, although relatively little is known about UGT2B11 and UGT2B28 compared to other UGT2B family members, these enzymes have been suggested to heterodimerize and inhibit androgen-metabolizing UGT2B enzymes, thereby preventing androgen inactivation and clearance [95]. In agreement with these findings, reanalysis of RNA-Seq data from TCGA PRAD cohorts revealed a significant downregulation of UGT2B7 transcripts, while UGT2B-11 and -28 expressions were significantly elevated in tumor samples (Figure 7E, F). Pearson correlation analysis of TCGA PRAD data revealed a

weak but significant negative association among DUOX1 with UGT2B-11 and -28 expressions (Figure 7G), which was further validated by qPCR analysis in DUOX1 stably expressing LNCaP cells (Figure 7H), reinforcing the link between impaired glucuronidation and DUOX1-associated transcriptional reprograming of AR signalling. ChIP-Seq data in DHT stimulated LNCaP cells demonstrated enriched AR signals on the promoter region of UGT2B-15, -17, -11 and -28 genes (Figures 7I and S17). Reanalysis of transcriptomics data of androgen stimulated and deprived LNCaP cells revealed in contrast to UGT2B-15 and -17, AR positively regulates UGT2B-11 and -28 expressions (Figure 7J-K). ChIP-qPCR analysis further validated that AR was significantly enriched onto the promoter region of UGT2B28 only in response to androgen stimulation in LNCaP-DUOX1 cells (Figure 7L). However, DUOX1 overexpression upon DOX treatment markedly attenuated AR recruitment (Figure 7L), thereby suppressing UGT2B28 transcription (Figure 7H). Consequently, DHT-specific competitive ELISA demonstrated that DUOX1 overexpression in LNCaP cells growing in normal media significantly enhanced DHT clearance (Figure 7M). Similar experimental set up of DUOX1 stably expressing LNCaP cells growing in media supplemented with charcoal stripped serum (CSS) did not show any detectable DHT (Figure 7M), further validating DUOX1 mediated DHT clearance from PCa cells. The deregulated expression profile of UGT2B members upon DUOX1 restoration suggests impaired androgen conjugation capacity, which may disrupt the feedback control of AR signalling and thereby affecting PCa pathogenesis (Figure 7N).

Discussion

PCa progression is driven by a complex interplay of genetic, epigenetic, and transcriptional alterations that converge on key oncogenic pathways, particularly AR signalling [7,11]. Among the various epigenetic regulations, aberrant DNA methylation has emerged as a critical driver during PCa development [11,12]. In this study, we identify DUOX1 as a methylation-driven tumor suppressor biomarker whose repression is governed by coordinated epigenetic and AR-dependent transcriptional mechanisms.

Consistent with previous reports highlighting promoter hypermethylation as a hallmark of TSG inactivation in PCa [13-19], our genome-wide methylation profiling of BPH and PCa patients' tissue biopsy samples, coupled with analysis of TCGA dataset, identified DUOX1 as one of the most significantly hypermethylated genes in PCa. Reduced DUOX1 expression is associated with more aggressive disease, characterized by higher Gleason score, and poorer survival, underscoring its potential as a biomarker of PCa progression and adverse clinical outcome. DNMTs act as DNA-methylation writers that negatively regulate transcriptions of multiple TSGs, thereby contributing to cancer development, including PCa [47,48]. Among the three major DNMTs, DNMT1 functions primarily as a maintenance methyltransferase, methylating hemimethylated DNA during replication, whereas DNMT3A and DNMT3B serve as *de novo* methyltransferases that establish new methylation patterns on previously unmethylated DNA [46]. Both DNMT3A and DNMT3B are frequently upregulated in PCa and contribute to disease progression, metastasis, and the emergence of CRPC through epigenetic silencing of TSGs. Notably, loss of DNMT3A or DNMT3B is associated with global hypomethylation, whereas DNMT3B overexpression promotes hypermethylation in multiple cancer types [46-48]. In line with these observations, our study demonstrates that DNMT3A and DNMT3B act as key regulators of DUOX1 promoter hypermethylation and transcriptional repression. Our findings reinforce the established role of DNMTs in cancer-associated epigenetic remodeling and further implicate *de novo* DNMTs as critical determinants of DUOX1 silencing in PCa.

Beyond epigenetic silencing, our findings uncover a direct role for AR in repressing DUOX1 transcription. AR signalling constitutes a central regulatory axis in both normal prostate physiology and PCa development [51,52]. Deregulation of the AR signalling cascade drives the transition from localized disease to CRPC, where AR activity is paradoxically sustained despite hormone deprivation therapy [52-54]. Although anti-androgen therapy remains first-line treatment for advanced disease, therapeutic resistance inevitably emerges, underscoring the persistent reliance of tumor cells on AR-driven transcriptional programs. Importantly, accumulating evidence indicates AR exhibits context-dependent functions, acting not only as a transcriptional activator but also as a repressor, thereby shaping PCa pathogenesis [55-57]. Herein we identify DUOX1 as a novel target of AR-mediated transcriptional repression. Our findings demonstrate that AR directly occupies an intragenic regulatory region within the DUOX1 locus and suppresses its expression in a DNA-binding-dependent manner. FOXA1, a pioneer transcription factor, is known to facilitate AR chromatin access by promoting chromatin decompaction and modulating AR binding dynamics [56]. Moreover, FOXA1 reduces AR availability to specific ARE sites by expediting AR binding to several low affinity ARE sites located within the proximity of FOXA1 binding sites, thereby affecting tumor progression when both AR and FOXA1 concentrations are in equilibrium [56]. However, our findings indicate that AR-mediated repression of DUOX1 occurs independently of FOXA1 recruitment. The consistent inverse correlation between AR and DUOX1 expression across clinical and cell line datasets, and our experimental systems further supports the physiological relevance of this regulatory interaction. Collectively, our results expand the current understanding of AR signalling by revealing its role in repressing a redox-regulating gene, thereby contributing to PCa progression.

Further mechanistic investigation into androgen-induced, AR-dependent deregulation of DUOX1 transcription uncovered an enhancer-mediated repressive circuit involving H3K27ac and BRD4. H3K27ac is a well-established marker of active enhancers and promoters, facilitating transcription by promoting an open chromatin configuration and distinguishing active regulatory regions from poised or inactive genomic elements [66,67]. Notably, H3K27ac has been implicated in

PCa pathogenesis, with a substantial proportion of disease-associated regulatory elements residing within H3K27ac-marked regions [76]. Our findings suggest that, during PCa progression, H3K27ac occupancy is redistributed from the DUOX1 promoter to AR-bound enhancer regions, thereby promoting BRD4 recruitment and reinforcing AR-mediated transcriptional repression of DUOX1. BRD4, a key epigenetic reader of acetylated histones, regulates oncogenic transcription by recruiting transcriptional machinery to active chromatin regions [63-65]. In particular, H3K27ac-enriched enhancers serve as major platforms for BRD4 binding and activity [68]. Consistent with this, pharmacological inhibition of BRD4 has emerged as a promising therapeutic strategy in advanced PCa and CRPC, in part through disruption of AR chromatin binding and transcriptional activity [69-72]. In line with this, our model suggests that the H3K27ac-BRD4-AR axis establishes a repressive chromatin environment at the DUOX1 locus, effectively silencing its expression while simultaneously promoting AR-driven oncogenic programs. In addition to AR, BRD4 positively regulates MYC transcription [73,74]. Our results also demonstrate that BRD4 inactivation specifically downregulates MYC expression. However, whether MYC contributes directly to DUOX1 repression warrants further investigation.

Accumulating evidence indicates that DUOX1 is frequently downregulated through promoter hypermethylation across multiple solid malignancies, including breast, hepatocellular and lung carcinomas [28-31]. Consistently, our pan-cancer analysis of TCGA datasets revealed significant downregulation of DUOX1 in half of the examined tumor types, including PCa, supporting its role as a putative tumor suppressor. Functionally, restoration of DUOX1 expression in PCa cells exerted pronounced anti-tumor and anti-metastatic effects, primarily through modulation of redox homeostasis. As a member of the NOX family, DUOX1 generates ROS, particularly extracellular H_2O_2, thereby contributing to redox-dependent signalling [23,82]. Emerging evidence suggests that DUOX1-derived H_2O_2 plays context-dependent roles in tumorigenesis. For example, radiation-induced upregulation of DUOX1 has been implicated in thyroid carcinogenesis by sustaining oxidative signalling under genotoxic stress [32], whereas in neuroblastoma cells, ROS have been shown to maintain DUOX1 and DUOX2 expression, suggesting a feedback loop between redox signalling and DUOX

enzyme regulation [33]. These observations collectively highlight the context-specific and multifaceted role of DUOX1 in cancer biology. In line with this, our data demonstrate that re-expression of DUOX1 in PCa cells leads to increased ROS production and induction of apoptosis, consistent with the well-established dual role of ROS in cancer, wherein low levels promote survival while elevated levels trigger cell death [85]. AR-mediated suppression of DUOX1 therefore likely contributes to maintaining a pro-tumorigenic redox balance. Notably, moderate ROS levels have been reported to enhance AR signalling, whereas excessive ROS can suppress AR expression [85-87], supporting the existence of a feedback loop in which DUOX1-derived ROS negatively regulate AR activity. To our knowledge, this study provides the first evidence that DUOX1 functions as a negative regulator of AR signalling in PCa. In addition to redox regulation, DUOX1 appears to influence androgen metabolism. Our transcriptomic analysis revealed that restoration of DUOX1 alters the expression of UGT2B family members involved in androgen inactivation and clearance [94,95]. Notably, UGT2B11 and UGT2B28 can heterodimerize to inhibit androgen-metabolizing UGT2B enzymes, thereby sustaining intracellular androgen availability [95]. These findings support a model in which DUOX1-mediated modulation of the glucuronidation pathway disrupts androgen homeostasis and attenuates AR-driven tumor growth.

Beyond its role as a biomarker, our findings support DUOX1 as a therapeutically actionable target in PCa. Restoration of DUOX1 expression through inhibition of *de novo* DNMTs and/or disruption of the H3K27ac-BRD4-AR axis, may represent an effective strategy to counteract AR-driven oncogenic programs. Notably, DNA-methylation inhibitors such as azacytidine and anti-androgens such as enzalutamide are already in clinical use or under evaluation for PCa treatment [44,45,58,59]. Moreover, BET bromodomain inhibitors targeting BRD4 have demonstrated significant anti-tumor efficacy in preclinical models of CRPC [70-72]. Interestingly, our results demonstrated that combined epigenetic and AR-targeted interventions did not produce additive effects on DUOX1 expression compared to individual treatments, suggesting convergence on a shared regulatory pathway.

Consistent with this notion, prolonged azacytidine treatment has been reported to restore AR expression and sensitize AR-negative PCa cells to hormonal therapy [45,96].

Despite the mechanistic framework established in this study, several important questions remain unanswered. The precise molecular determinants governing AR-mediated transcriptional repression at the DUOX1 locus require further investigation. Emerging evidence suggests that hyperactive AR signalling reshapes the PCa transcriptome, in part through widespread modulation of alternative splicing, thereby contributing to disease progression and resistance to anti-androgen therapies [97]. In this context, our preliminary bioinformatic analysis indicate that AR recruitment to the intragenic DUOX1 locus may promote alternative splicing events, potentially generating an N-terminally truncated DUOX1 isoform lacking a portion of the peroxidase domain required for H_2O_2 production. The functional consequences of this putative isoform, whether inactive or tumor-promoting, warrant further in-depth investigation. Furthermore, the dual role of ROS in mediating both tumor-suppressive and tumor-promoting effects suggests that the impact of DUOX1 reactivation may be highly context-dependent [81,85]. In addition, AR signalling and PCa stemness exhibit an inverse relationship, with reduced AR activity linked to enhanced stem-like features and therapeutic resistance [92,93]. Consistent with this, our findings indicate that both DUOX1 restoration and anti-androgen treatment may promote stemness-associated phenotypes. Collectively, our findings highlight the complexity of the AR-DUOX1 regulatory axis and further emphasise the need for carefully designed therapeutic strategies.

In summary, our study positions DUOX1 at the nexus of epigenetic regulation, transcriptional control, and metabolic reprogramming in PCa, underscoring its potential as both a clinically relevant biomarker and a therapeutic target. While our findings provide a mechanistic framework linking DNMT3A/3B- and AR-driven repression to redox signalling pathways, further validation in *in vivo* models and larger, well-characterized patient cohorts will be essential to establish the translational relevance of DUOX1 in PCa management.

Data availability

850K Methylation array datasets of 16 prostate tissue biopsy samples and RNA-Seq datasets of LNCaP cells stably expressing DUOX1 have been submitted to GEO repository with accession number GSE241670 and GSE326702, respectively. All data generated and analysed in this study are included in the manuscript and supporting files. The original data of western blot and qPCR analyses are available under the supplemental material category.

Acknowledgements

We sincerely thank to Erle S Robertson (Perelman School of Medicine, University of Pennsylavania, USA), Arthur Riggs (Beckman Research Institute of the City of Hope, USA), Didier Trono (Ecole Polytechnique Fédérale de Lausanne, Switzerland), Simon Davis (University of Oxford, UK), Michael Mancini (Baylor College of Medicine, USA), Debrya Groskreutz (Promega Corp., USA), Feng Zhang (Massachusetts Institute of Technology, USA), William Hahn (Dana-Farber Cancer Institute and Harvard Medical School, USA) and National Centre for Cell Science (NCCS), Dept. of Biotechnology (DBT), Govt. of India for providing reagents, plasmids, and cell lines. We are also thankful to late Dilip Kumar Pal, Professor, Department of Urology, Institute of Post Graduate Medical Education and Research, Kolkata for his support and assistance in collection of clinical samples.

Author contributions

SN and AS conceived the study. SN, PS, SM, SD, JB, SKAA, SA, AB, KB, KM, AG, AK, DM, and PM performed the experiments and data analyses. AB, KB, KM and AG collected the patients' samples. SN, PS, SM, SoN, PM and AS analysed and interpreted the data. SN and AS wrote the manuscript. All the authors reviewed and approved the final version of the manuscript.

Funding

This work was supported partly by grants from DBT/Wellcome Trust India Alliance (IA/I/14/2/501537) and Dept. Science & Technology and Biotechnology (DST-BT), Govt. of West Bengal (ST/P/S&T/9G-5/2019) and Council of Scientific and Industrial Research (CSIR), Govt. of India (37/1749/EMR-II) to AS. The funders had no role in study design, data collection and analysis, decision to publish, or preparation of the manuscript.

Conflict of interest statement

None declared.

References

1. Bray F, Ferlay J, Soerjomataram I, Siegel Rl, Torre La, Jemal A. Global cancer statistics 2018: GLOBOCAN estimates of incidence and mortality worldwide for 36 cancers in 185 countries. *CA Cancer J Clin* 68(6), 394-424 (2018).
2. Rawla P. Epidemiology of Prostate Cancer. *World J Oncol* 10(2), 63-89 (2019).
3. St John J, Powell K, Conley-Lacomb MK, Chinni SR. TMPRSS2-ERG Fusion Gene Expression in Prostate Tumor Cells and Its Clinical and Biological Significance in Prostate Cancer Progression. *J Cancer Sci Ther* 4(4), 94-101 (2012).
4. Hawksworth D, Ravindranath L, Chen Y *et al*. Overexpression of C-MYC oncogene in prostate cancer predicts biochemical recurrence. *Prostate Cancer Prostatic Dis* 13(4), 311-315 (2010).
5. Jamaspishvili T, Berman DM, Ross AE *et al*. Clinical implications of PTEN loss in prostate cancer. *Nat Rev Urol* 15(4), 222-234 (2018).
6. Ecke TH, Schlechte HH, Schiemenz K *et al*. TP53 gene mutations in prostate cancer progression. *Anticancer Res* 30(5), 1579-1586 (2010).
7. Morova T, Mcneill DR, Lallous N *et al*. Androgen receptor-binding sites are highly mutated in prostate cancer. *Nat Commun* 11(1), 832 (2020).
8. Sopyllo K, Erickson AM, Mirtti T. Grading Evolution and Contemporary Prognostic Biomarkers of Clinically Significant Prostate Cancer. *Cancers (Basel)* 13(4), (2021).
9. Sumanasuriya S, De Bono J. Treatment of Advanced Prostate Cancer-A Review of Current Therapies and Future Promise. *Cold Spring Harb Perspect Med* 8(6), (2018).
10. Litwin MS, Tan HJ. The Diagnosis and Treatment of Prostate Cancer: A Review. *JAMA* 317(24), 2532-2542 (2017).
11. Massie CE, Mills IG, Lynch AG. The importance of DNA methylation in prostate cancer development. *J Steroid Biochem Mol Biol* 166 1-15 (2017).
12. Zelic R, Fiano V, Grasso C *et al*. Global DNA hypomethylation in prostate cancer development and progression: a systematic review. *Prostate Cancer Prostatic Dis* 18(1), 1-12 (2015).
13. Chen Y, Li J, Yu X *et al*. APC gene hypermethylation and prostate cancer: a systematic review and meta-analysis. *Eur J Hum Genet* 21(9), 929-935 (2013).
14. Liu L, Yoon JH, Dammann R, Pfeifer GP. Frequent hypermethylation of the RASSF1A gene in prostate cancer. *Oncogene* 21(44), 6835-6840 (2002).
15. Song JZ, Stirzaker C, Harrison J, Melki JR, Clark SJ. Hypermethylation trigger of the glutathione-S-transferase gene (GSTP1) in prostate cancer cells. *Oncogene* 21(7), 1048-1061 (2002).
16. Tang D, Kryvenko ON, Mitrache N *et al*. Methylation of the RARB gene increases prostate cancer risk in black Americans. *J Urol* 190(1), 317-324 (2013).
17. Verdoodt B, Sommerer F, Palisaar RJ *et al*. Inverse association of p16 INK4a and p14 ARF methylation of the CDKN2a locus in different Gleason scores of prostate cancer. *Prostate Cancer Prostatic Dis* 14(4), 295-301 (2011).
18. Gurioli G, Salvi S, Martignano F *et al*. Methylation pattern analysis in prostate cancer tissue: identification of biomarkers using an MS-MLPA approach. *J Transl Med* 14(1), 249 (2016).
19. Bjerre MT, Strand SH, Norgaard M *et al*. Aberrant DOCK2, GRASP, HIF3A and PKFP Hypermethylation has Potential as a Prognostic Biomarker for Prostate Cancer. *Int J Mol Sci* 20(5), (2019).

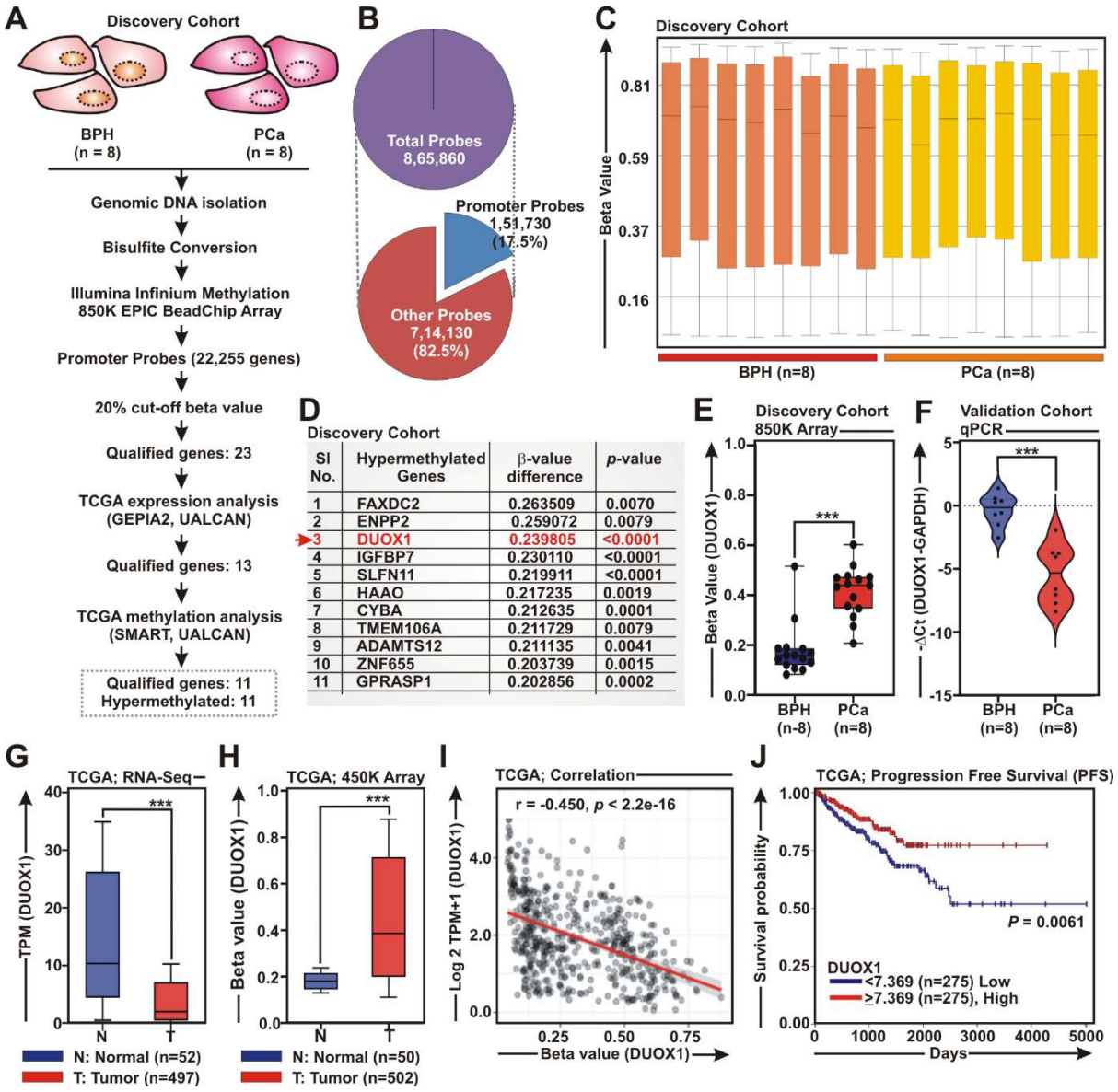
20. Kirby MK, Ramaker RC, Roberts BS *et al*. Genome-wide DNA methylation measurements in prostate tissues uncovers novel prostate cancer diagnostic biomarkers and transcription factor binding patterns. *BMC Cancer* 17(1), 273 (2017).
21. Nikas JB, Nikas EG. Genome-Wide DNA Methylation Model for the Diagnosis of Prostate Cancer. *ACS Omega* 4(12), 14895-14901 (2019).
22. Luo JH, Ding Y, Chen R *et al*. Genome-wide methylation analysis of prostate tissues reveals global methylation patterns of prostate cancer. *Am J Pathol* 182(6), 2028-2036 (2013).
23. Vermot A, Petit-Hartlein I, Smith SME, Fieschi F. NADPH Oxidases (NOX): An Overview from Discovery, Molecular Mechanisms to Physiology and Pathology. *Antioxidants (Basel)* 10(6), (2021).
24. Alfadda AA, Sallam RM. Reactive oxygen species in health and disease. *J Biomed Biotechnol* 2012 936486 (2012).
25. Graham KA, Kulawiec M, Owens KM *et al*. NADPH oxidase 4 is an oncoprotein localized to mitochondria. *Cancer Biol Ther* 10(3), 223-231 (2010).
26. You X, Ma M, Hou G, Hu Y, Shi X. Gene expression and prognosis of NOX family members in gastric cancer. *Onco Targets Ther* 11 3065-3074 (2018).
27. Zhang X, Han J, Feng L *et al*. DUOX2 promotes the progression of colorectal cancer cells by regulating the AKT pathway and interacting with RPL3. *Carcinogenesis* 42(1), 105-117 (2021).
28. Chen S, Ling Q, Yu K *et al*. Dual oxidase 1: A predictive tool for the prognosis of hepatocellular carcinoma patients. *Oncol Rep* 35(6), 3198-3208 (2016).
29. Fortunato RS, Gomes LR, Munford V *et al*. DUOX1 Silencing in Mammary Cell Alters the Response to Genotoxic Stress. *Oxid Med Cell Longev* 2018 3570526 (2018).
30. Little AC, Sham D, Hristova M *et al*. DUOX1 silencing in lung cancer promotes EMT, cancer stem cell characteristics and invasive properties. *Oncogenesis* 5(10), e261 (2016).
31. Luxen S, Belinsky SA, Knaus UG. Silencing of DUOX NADPH oxidases by promoter hypermethylation in lung cancer. *Cancer Res* 68(4), 1037-1045 (2008).
32. Ameziane-El-Hassani R, Talbot M, De Souza Dos Santos MC *et al*. NADPH oxidase DUOX1 promotes long-term persistence of oxidative stress after an exposure to irradiation. *Proc Natl Acad Sci U S A* 112(16), 5051-5056 (2015).
33. Damiano S, Fusco R, Morano A *et al*. Reactive oxygen species regulate the levels of dual oxidase (Duox1-2) in human neuroblastoma cells. *PLoS One* 7(4), e34405 (2012).
34. Pettigrew CA, Clerkin JS, Cotter TG. DUOX enzyme activity promotes AKT signalling in prostate cancer cells. *Anticancer Res* 32(12), 5175-5181 (2012).
35. Holl M, Koziel R, Schafer G *et al*. ROS signaling by NADPH oxidase 5 modulates the proliferation and survival of prostate carcinoma cells. *Mol Carcinog* 55(1), 27-39 (2016).
36. Sarkar P, Malik S, Banerjee A *et al*. Differential Microbial Signature Associated With Benign Prostatic Hyperplasia and Prostate Cancer. *Front Cell Infect Microbiol* 12, 894777 (2022).
37. Malik S, Biswas J, Sarkar P *et al*. Differential carbonic anhydrase activities control EBV-induced B-cell transformation and lytic cycle reactivation. *PLoS Pathog* 20(3), e1011998 (2024).
38. Siegel RL, Miller KD, Jemal A. Cancer statistics, 2016. *CA Cancer J Clin* 66(1), 7-30 (2016).
39. Geybels MS, Wright JL, Bibikova M *et al*. Epigenetic signature of Gleason score and prostate cancer recurrence after radical prostatectomy. *Clin Epigenetics* 8, 97 (2016).
40. Wu J-X, Liu R, Song K *et al*. Structures of human dual oxidase 1 complex in low-calcium and high-calcium states. *Nat Commun* 12(1), 155 (2021).

41. Walia A, Tuia J, Prasad V. Progression-free survival, disease-free survival and other composite end points in oncology: improved reporting is needed. *Nat Rev Clin Oncol* 20(12), 885-895 (2023).
42. Oh EL, Huish W, El-Gamil S *et al*. Assessment of Patient and Clinician Perspectives on Clinically Meaningful Extension of Progression-free Survival in Prostate Cancer. *Eur Urol Open Sci* 70, 175-182 (2024).
43. Fialova B, Luzna P, Gursky J et al. Epigenetic modulation of AR gene expression in prostate cancer DU145 cells with the combination of sodium butyrate and 5'-Aza-2'-deoxycytidine. Oncol Rep 36(4), 2365-74 (2016).
44. Festuccia C, Gravina GL, D'Alessandro AM *et al*. Azacitidine improves antitumor effects of docetaxel and cisplatin in aggressive prostate cancer models. *Endocr Relat Cancer* 16(2), 401-13 (2009).
45. Sonpavde G, Aparicio A, Guttierez I *et al.* Phase II study of azacitidine to restore responsiveness of prostate cancer to hormonal therapy. *Clin Genitourin Cancer* 5(7), 457-9 (2007).
46. Zhang J, Yang C, Wu C *et al*. DNA Methyltransferases in Cancer: Biology, Paradox, Aberrations, and Targeted Therapy. *Cancers (Basel)* 12(8), 2123 (2020).
47. Nishiyama A, Nakanishi M. Navigating the DNA methylation landscape of cancer. *Trends Genet* 37(11), 1012-1027 (2021).
48. Shin HJ, Hua JT, Li H. Recent advances in understanding DNA methylation of prostate cancer. *Front Oncol* 13, 1182727 (2023).
49. Spans L, Helsen C, inckemalie L *et al*. Comparative genomic and transcriptomic analyses of LNCaP and C4-2B prostate cancer cell lines. *PLoS One* 9(2), e90002 (2014).
50. Yu J, Chai X, Pang J *et al*. Discovery of novel non-nucleoside inhibitors with high potency and selectivity for DNA methyltransferase 3A. *Eur J Med Chem* 242, 114646 (2022).
51. Fujita K, Nonomura N. Role of Androgen Receptor in Prostate Cancer: A Review. *World J Mens Health* 37(3), 288–295 (2018).
52. Sharma NL, Massie CE, Ramos-Montoya A *et al*. The androgen receptor induces a distinct transcriptional program in castration-resistant prostate cancer in man. *Cancer Cell* 23(1), 35-47 (2013).
53. Karantanos T, Corn PG, Thompson TC. Prostate cancer progression after androgen deprivation therapy: mechanisms of castrate resistance and novel therapeutic approaches. *Oncogene* 32(49), 5501-11 (2013).
54. Montgomery RB, Mostaghel EA, Vessella R *et al*. Maintenance of intratumoral androgens in metastatic prostate cancer: a mechanism for castration-resistant tumor growth. *Cancer Res* 68(11), 4447-54 (2008).
55. Wang Q, Li W, Liu XS et al. A hierarchical network of transcription factors governs androgen receptor-dependent prostate cancer growth. *Mol Cell* 27(3), 380-92 (2007).
56. Jin H-J, Zhao JC, Wu L *et al*. Cooperativity and equilibrium with FOXA1 define the androgen receptor transcriptional program. *Nat Commun* 30(5), 3972 (2014).
57. Tiwari R, Manzar N, Bhatia V *et al*. Androgen deprivation upregulates SPINK1 expression and potentiates cellular plasticity in prostate cancer. *Nat Commun* 11(1), 384 (2020).
58. Davis ID, Martin AJ, Stockler MR et al. Enzalutamide with Standard First-Line Therapy in Metastatic Prostate Cancer. N Engl J Med 381(2), 121-131 (2019).
59. Penson DF, Armstrong AJ, Concepcion R et al. Enzalutamide Versus Bicalutamide in Castration-Resistant Prostate Cancer: The STRIVE Trial. J Clin Oncol 34(18), 2098-106 (2016).

60. Rauluseviciute I, Riudavets-Puig R, Blanc-Mathieu R *et al*. JASPAR 2024: 20th anniversary of the open-access database of transcription factor binding profiles. *Nucleic Acids Res* 52(D1), D174-D182 (2024).
61. Massie CE, Adryan B, Barbosa-Morais NL et al. New androgen receptor genomic targets show an interaction with the ETS1 transcription factor. EMBO Rep 8(9), 871-8 (2007).
62. Cai C, He HH, Gao S *et al*. Lysine-specific demethylase 1 has dual functions as a major regulator of androgen receptor transcriptional activity. *Cell Rep* 9(5), 1618-1627 (2014).
63. Morozov VM, Riva A, Sarwar S *et al*. HIRA-mediated loading of histone variant H3.3 controls androgen-induced transcription by regulation of AR/BRD4 complex assembly at enhancers. *Nucleic Acids Res* 51(19), 10194-10217 (2023).
64. Loven J, Hoke HA, Lin CY *et al*. Selective inhibition of tumor oncogenes by disruption of super-enhancers. *Cell* 153, 320-334 (2013).
65. Hnisz D, Abraham BJ, Lee TI *et al*. Super-enhancers in the control of cell identity and disease. *Cell* 155, 934-947 (2013).
66. Creyghton MP, Cheng AW, Welstead GG *et al*. Histone H3K27ac separates active from poised enhancers and predicts developmental state. *Proc Natl Acad Sci USA* 107, 21931-21936 (2010).
67. Rada-Iglesias A, Bajpai R, Swigut T *et al*. A unique chromatin signature uncovers early developmental enhancers in humans. *Nature* 470, 279-283 (2011).
68. Jahangiri L, Tsaprouni L, Trigg RM *et al*. Core regulatory circuitries in defining cancer cell identity across the malignant spectrum. *Open Biol* 10, 200121 (2020).
69. Asangani IA, Dommeti VL, Wang X *et al*. Therapeutic targeting of BET bromodomain proteins in castration-resistant prostate cancer. *Nature*; 510, 278-282 (2014).
70. Leiming W, Mafei X, Chung-Yang K *et al*. Small molecule JQ1 promotes prostate cancer invasion via BET-independent inactivation of FOXA1. *J Clin Invest* 130(4), 1782-1792 (2020).
71. Irfan AA, Vijaya LD, Xiaoju W *et al*. Therapeutic targeting of BET bromodomain proteins in castration-resistant prostate cancer. *Nature* 510(7504), 278-82 (2014).
72. Shipra S, Dan L, Woo HC *et al*. BET inhibitors reduce tumor growth in preclinical models of gastrointestinal gene signature–positive castration-resistant prostate cancer. *J Clin Invest* 135(16), e180378 (2025).
73. Jake ED, Ghayas CI, Madeleine EL *et al*. BET bromodomain inhibition as a therapeutic strategy to target c-Myc. *Cell* 146(6), 904-17 (2011).
74. Jennifer AM, Andrew RC, Barbara MB *et al*. Targeting MYC dependence in cancer by inhibiting BET bromodomains. *Proc Natl Acad Sci USA* 108(40), 16669-74 (2011).
75. Yifan T, Lei W, Yang D *et al*. Inhibition of BRD4 suppresses tumor growth in prostate cancer via the enhancement of FOXO1 expression. *Int J Oncol* 53(6), 2503-2517 (2018).
76. Alexander G, Huwenbo S, Gleb K *et al*. Atlas of prostate cancer heritability in European and African-American men pinpoints tissue-specific regulation. *Nat Commun* 7, 10979 (2016).
77. Philip AW, Katharine E-Y, Jennifer CK *et al*. Context-dependent hormone-refractory progression revealed through characterization of a novel murine prostate cancer cell line. *Cancer Res* 65(24), 11565-71 (2005).
78. Marek L, Malgorzata M, Davide F *et al*. Activation and Caspase-mediated Inhibition of PARP: A Molecular Switch between Fibroblast Necrosis and Apoptosis in Death Receptor Signaling. *Mol Biol Cell* 13(3), 978-988 (2002).
79. Saquib AL, Ali M, Keisuke K *et al*. Caspases 3 and 7: Key Mediators of Mitochondrial Events of Apoptosis. *Science* 311(5762), 847-851 (2006).

80. Hui W, Haowei L, Yige W. Knockdown of Dual Oxidase 1 (DUOX1) Promotes Wound Healing by Regulating Reactive Oxygen Species (ROS) by Activation of Nuclear Factor kappa B (NF-κB) Signaling. *Med Sci Monit* 27, e926492-1-e926492-11 (2021).
81. Zhiwei W, Yiwei L, Fazlul HS. Signaling Mechanism(S) of Reactive Oxygen Species in Epithelial-Mesenchymal Transition Reminiscent of Cancer Stem Cells in Tumor Progression. *Curr Stem Cell Res Ther* 5(1), 74-80 (2010).
82. Geiszt M, Witta J, Baffi J *et al*. Dual oxidases represent novel hydrogen peroxide sources supporting mucosal surface host defense. *FASEB J* 17(11), 1502-4 (2003).
83. Sergey D. Crosstalk between mitochondria and NADPH oxidases. *Free Radic Biol Med* 51(7), 1289-1301 (2011).
84. Li P, Nicosia SV, Bai W. Antagonism between PTEN/MMAC1/TEP-1 and androgen receptor in growth and apoptosis of prostatic cancer cells. *J Biol Chem* 276(23), 20444-50 (2001).
85. Chenglin H, Zilong W, Yingkun X *et al*. Roles of Reactive Oxygen Species in Biological Behaviors of Prostate Cancer. *Biomed Res Int* 2020, 1269624 (2020).
86. Khurana N, Chandra PK, Kim H *et al*. Bardoxolone-Methyl (CDDO-Me) Suppresses Androgen Receptor and Its Splice-Variant AR-V7 and Enhances Efficacy of Enzalutamide in Prostate Cancer Cells. *Antioxidants (Basel)* 9(1), 68 (2020).
87. Hua X, Yin S, Chi-Ping H *et al*. Preclinical Study Using ABT263 to Increase Enzalutamide Sensitivity to Suppress Prostate Cancer Progression Via Targeting BCL2/ROS/USP26 Axis Through Altering ARv7 Protein Degradation. *Cancers (Basel)* 12(4):831 (2020).
88. Fridovich I. Superoxide radical and superoxide dismutases. *Annu Rev Biochem* 64, 97-112 (1995).
89. Christophe G, Pedro BC. Targeting catalase in cancer. *Redox Biol* 77, 103404 (2024).
90. Yi L, Yicong W, Yi J *et al*. GPX4: The hub of lipid oxidation, ferroptosis, disease and treatment. *Biochim Biophys Acta Rev Cancer* 1878(3), 188890 (2023).
91. Lili H, Guangli C, Jing H *et al*. ZC3H13 reduced DUOX1-mediated ferroptosis in laryngeal squamous cell carcinoma cells through m6A-dependent modification. *Tissue Cell* 84, 102187 (2023).
92. Anne S, Andreas H, Gregory C *et al*. Loss of Androgen Receptor Expression Promotes a Stem-Like Cell Phenotype in Prostate Cancer through STAT3 Signaling. *Cancer Res* 74(4), 1227-1237 (2013).
93. Changcheng G, Aimaitiaji K, Zhijin Z *et al*. ADT increases prostate cancer cell invasion via altering AR/SALL4/SOX2-OCT4 stem cell signaling. *Cell Biol Toxicol* 41(1), 107 (2025).
94. Alain B, Georges P, Fernand L *et al*. Inactivation of androgens by UDP-glucuronosyltransferase enzymes in humans. *Trends Endocrinol Metab* 14(10), 473-9 (2003).
95. Mackenzie P, Meyers J, Hulin J-A *et al*. Potential novel role of UDP glucuronosyltransferases 2B11 and 2B28 in crosstalk between androgen and lipid signalling. *FASEB J* 34, 1 (2020).
96. Gravina GL, Festuccia C, Millimaggi D *et al*. Chronic azacitidine treatment results in differentiating effects, sensitizes against bicalutamide in androgen-independent prostate cancer cells. *Prostate* 68(7), 793-801 (2008).
97. Shah K, Gagliano T, Garland L *et al*. Androgen receptor signaling regulates the transcriptome of prostate cancer cells by modulating global alternative splicing. *Oncogene* 39(39), 6172-6189 (2020).

Figure 1



Sl No.	Hypermethylated Genes	β-value difference	*p*-value
1	FAXDC2	0.263509	0.0070
2	ENPP2	0.259072	0.0079
3	DUOX1	0.239805	<0.0001
4	IGFBP7	0.230110	<0.0001
5	SLFN11	0.219911	<0.0001
6	HAAO	0.217235	0.0019
7	CYBA	0.212635	0.0001
8	TMEM106A	0.211729	0.0079
9	ADAMTS12	0.211135	0.0041
10	ZNF655	0.203739	0.0015
11	GPRASP1	0.202856	0.0002

Figure 1. Global methylation and TCGA analysis reveal DUOX1 as a methylation-driven biomarker for prostate cancer (PCa). (A) Workflow outlining genome-wide methylation profiling of 'discovery cohort' comprising of 8 BPH and 8 PCa biopsy samples using the Infinium MethylationEPIC 850K array. **(B)** Pie chart depicting promoter-embedded CpG sites in 850K methyl array. **(C)** Box plot showing differential promoter-embedded CpG sites between BPH and PCa samples ($p < 0.05$, FDR < 0.05). **(D)** Cross-comparison of 850K methyl array with TCGA-PRAD datasets identifying 11 hyper-methylated genes in PCa samples. **(E)** Box plot depicting increased DUOX1 promoter methylation in PCa compared to BPH in the 850K methylation array from the discovery cohort. **(F)** Violin plot showing reduced DUOX1 expression in PCa relative to BPH, as determined by qPCR analysis in the validation cohort. **(G)** RNA-Seq analysis showing DUOX1 mRNA expression in normal and tumor samples from the TCGA-PRAD dataset. **(H)** 450K methylation array data depicting DUOX1 promoter methylation levels in normal and tumor samples from the TCGA-PRAD dataset. **(I)** Pearson correlation analysis between DUOX1 promoter methylation and gene expression in the TCGA-PRAD dataset. **(J)** Kaplan-Meier survival analysis of patients stratified by high and low DUOX1 expression in the TCGA-PRAD dataset. Data were presented as the mean ± SD, n ≥ 3 biological replicates. Significant differences were shown (*** $p < 0.001$).

Figure 2

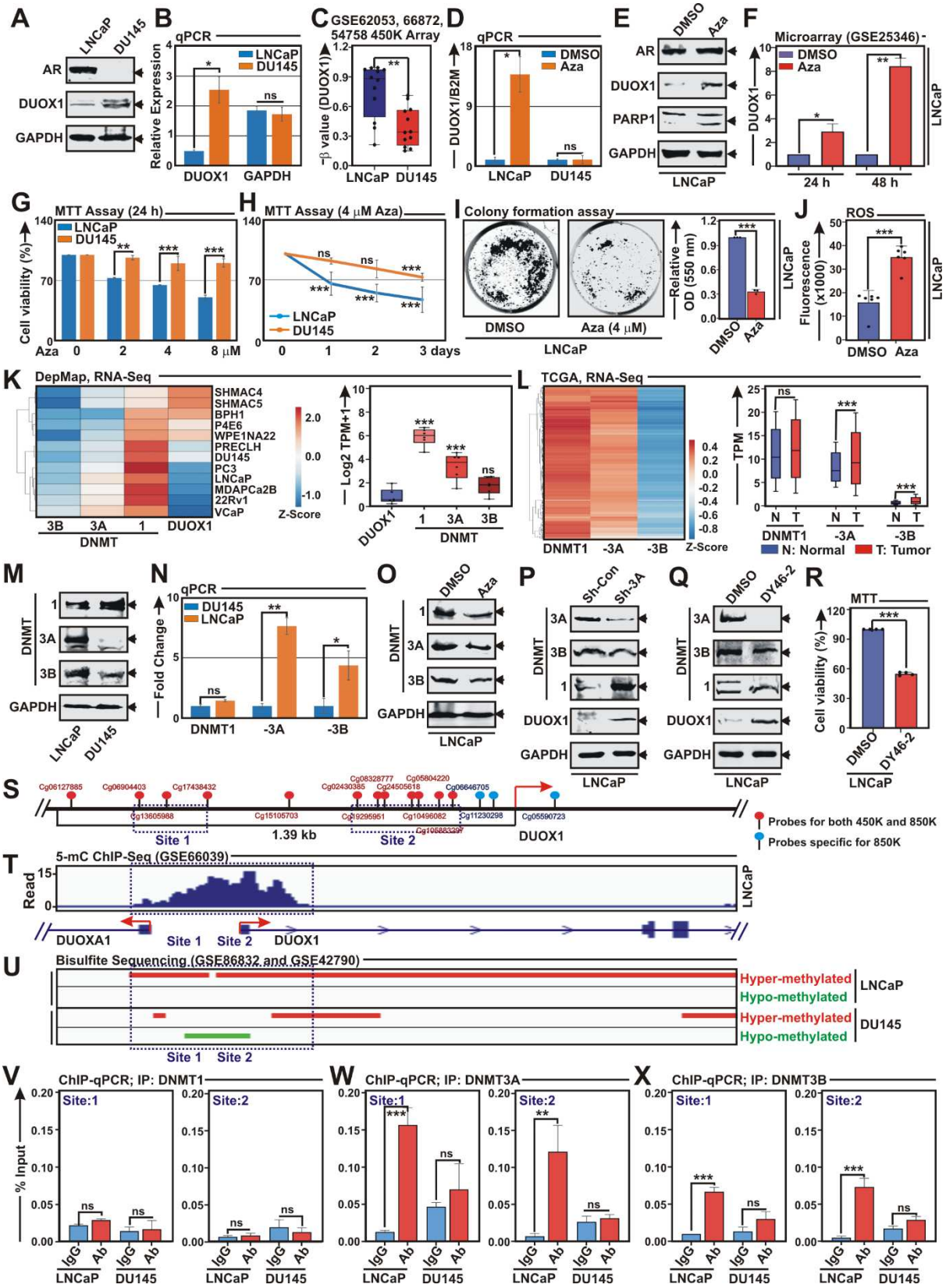


Figure 2. DNMT3A/3B-mediated promoter hypermethylation represses DUOX1 expression in androgen-sensitive PCa cells. (A) Western blot (WB) analysis of whole cell lysates (WCL) from LNCaP and DU145 cells. **(B)** qPCR showing relative expression of DUOX1 and GAPDH in LNCaP and DU145

cells. **(C)** 450K methyl array data (GSE62053, GSE66872 and GSE54758) showing DUOX1 promoter-methylation in LNCaP and DU145 cells. **(D)** qPCR showing relative DUOX1 expression in 4 µM 5-Aza-2-deoxycytidine (Aza)-treated LNCaP and DU145 cells for 48 h. **(E)** WB analysis of WCL from LNCaP cells with or without 4 µM Aza treatment for 48 h. **(F)** Reanalysis of microarray data (GSE25346) showing DUOX1 expression in LNCaP cells upon Aza treatment for 24-48 h. **(G)** MTT assay showing reduced viability of LNCaP compared with DU145 cells following Aza treatment with increasing concentrations (0-8 µM) for 24 h. **(H)** MTT assay showing reduced viability of LNCaP compared with DU145 cells following 4 µM Aza treatment for the indicated time points (0-3 days). **(I)** Colony formation assay showing decreased clonogenic potential of Aza-treated LNCaP cells. **(J)** DCFDA assay showing increased intracellular ROS in Aza-treated LNCaP cells. **(K)** Heatmap showing expression profiles of DNMT family members (DNMT1, DNMT3A, and DNMT3B) along with DUOX1 in DepMap RNA-Seq data from prostate cell lines (n = 12). Box plots (right) showing Pearson correlation between DNMT expression and DUOX1 levels in prostate adenocarcinoma cell lines (n = 6). **(L)** Heatmap and box plot showing expression of DNMTs in TCGA-PRAD RNA-Seq dataset. **(M)** WB analysis showing expression profile of DNMT members in LNCaP and DU145 cells. **(N)** qPCR showing mRNA expression profile of DNMT members in LNCaP and DU145 cells. **(O)** WB analysis showing expression of DNMTs in LNCaP cells with or without 4 µM Aza treatment for 48 h. **(P)** WB analysis showing the effect of DNMT3A knockdown (KD) in LNCaP cells stably expressing either control (Sh-Con) or DNMT3A specific (Sh-3A) Sh-RNAs. **(Q)** WB analysis showing the effect on LNCaP cells after 48 h treatment of vehicle control or 3 µM DNMT3A inhibitor DY-46-2. **(R)** MTT assay showing reduced viability of LNCaP cells following 3 µM DY-46-2 treatment for 48 h. **(S)** Pictorial representation of 15 CpG probes utilized in 450K and 850K methyl arrays within DUOX1 promoter region (red, probes for both 450K and 850K arrays; blue, probes specific for 850K array). **(T)** ChIP-Seq profile (GSE66039) showing enrichment of 5-methylcytosine (5mC) at the DUOX1 promoter region in LNCaP cells. The lower panel illustrates the DUOX1 gene structure, along with the positions of ChIP-qPCR primer sites (Site 1 and Site 2). **(U)** Bisulfite sequencing profiles (GSE86832 and GSE42790) showing the distribution of hypermethylated (red) and hypomethylated (green) regions across the DUOX1 gene locus in LNCaP and DU145 cells. **(V-X)** ChIP-qPCR analysis showing enrichment profiles of (V) DNMT1, (W) DNMT3A, and (X) DNMT3B at the DUOX1 promoter in LNCaP cells. Data were presented as the mean ± SD, n ≥ 3 biological replicates. Significant differences were shown (*$p < 0.05$; ** $p < 0.01$; *** $p < 0.001$; ns, not significant).

Figure 3

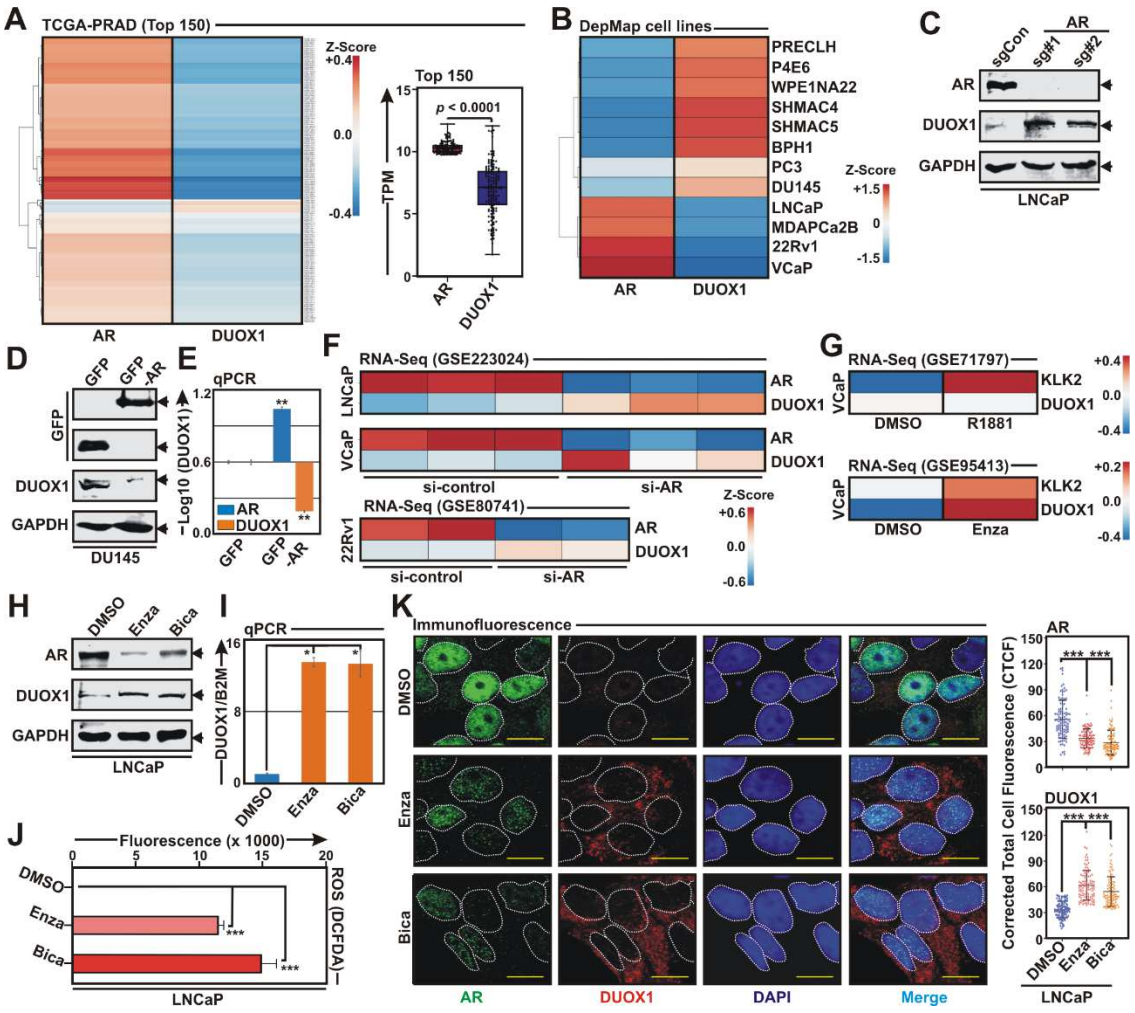


Figure 3. Androgen receptor (AR) signalling negatively regulates DUOX1 expression in PCa. (A) Heatmap showing RNA-Seq expression profiles of AR and DUOX1 in primary PCa samples from the TCGA-PRAD dataset (top 150 samples with high AR expression). The corresponding box plot (right) showing the inverse correlation between AR and DUOX1 expression. **(B)** Heatmap showing DUOX1 expression in DepMap prostate cell lines (n = 12), stratified based on AR expression levels. **(C)** WB analysis of WCL from LNCaP cells expressing the indicated sgRNAs. **(D)** WB analysis of WCL from DU145 cells transiently transfected with GFP or GFP-AR expression plasmids. **(E)** qPCR analysis showing relative expression of AR and DUOX1 transcripts in DU145 cells transiently transfected with GFP or GFP-AR expression plasmids. **(F)** Heatmaps showing relative mRNA expression of AR and DUOX1 in RNA-Seq datasets from control and AR knockdown conditions in LNCaP and VCaP cells (top; GSE223024) and 22Rv1 cells (bottom; GSE80741). **(G)** Heatmaps showing relative mRNA expression of KLK2 and DUOX1 in RNA-Seq datasets of VCaP cells following androgen stimulation with R1881 (top; GSE71797) or androgen deprivation with enzalutamide (Enza) (bottom; GSE95413). **(H)** WB analysis of WCL from LNCaP cells following androgen deprivation with Enza or bicalutamide (Bica). **(I)** qPCR analysis showing relative DUOX1 expression in LNCaP cells following treatment with Enza or Bica, as in (H). **(J)** DCFDA assay showing increased intracellular ROS levels in LNCaP cells following treatment with Enza or Bica. **(K)** Immunostaining of AR (green) and DUOX1 (red) in LNCaP cells following treatment with Enza or Bica. Nuclei were counterstained with DAPI. Scale bars, 5 µm. Dot plots of the same data (right) showing quantification of AR and DUOX1 corrected total cell fluorescence (CTCF). Data were presented as the mean ± SD, n ≥ 3 biological replicates. Significant differences were shown (*$p < 0.05$; ** $p < 0.01$; *** $p < 0.001$).

Figure 4

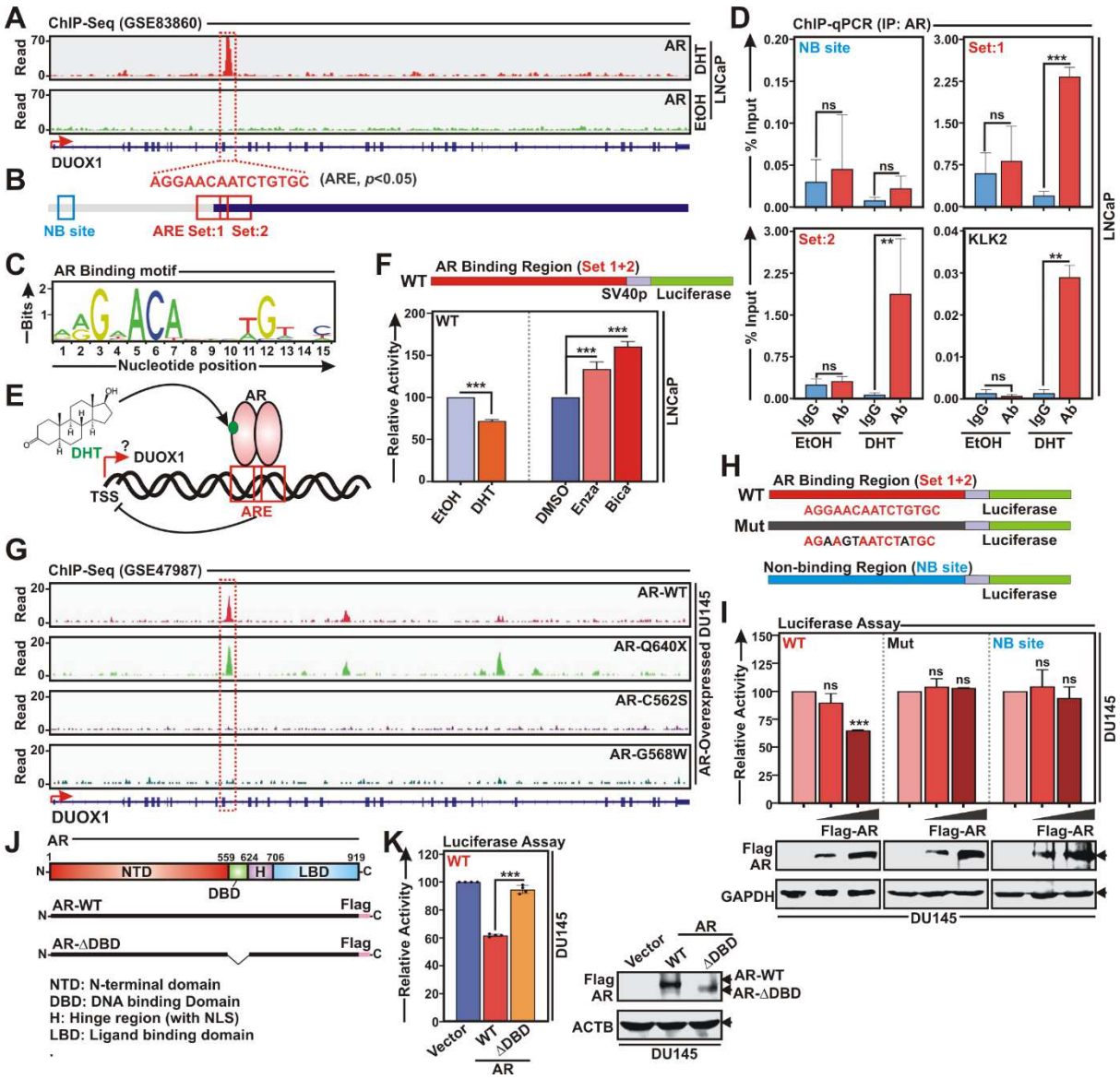


Figure 4. AR directly binds to an intragenic regulatory region to repress DUOX1 transcription. (A) AR ChIP-Seq tracks (GSE83860) in LNCaP cells showing AR occupancy at an intragenic enhancer region within the DUOX1 locus following androgen stimulation with dihydrotestosterone (DHT). **(B, C)** Schematic representations of (B) the DUOX1 gene locus highlighting the predicted androgen response element (ARE), and (C) the AR-binding motif obtained from the JASPAR database. **(D)** ChIP-qPCR analysis confirming androgen-induced AR binding to the DUOX1 enhancer region using two primer sets (1 and 2), but not to the non-binding (NB) site. Primers targeting AR binding at the KLK2 gene locus were used as a positive control. **(E)** Model illustrating androgen-dependent AR enrichment at the DUOX1 gene locus and its potential role in regulating DUOX1 transcription. **(F)** Schematic representation (top) of the DUOX1 luciferase reporter construct containing the AR enhancer region with the predicted ARE. Bar plots (bottom) showing luciferase reporter activity in LNCaP cells following DHT stimulation or treatment with Enza or Bica. **(G)** ChIP-Seq profiles (GSE47987) showing AR enrichment at the DUOX1 gene locus in DU145 cells overexpressing wild-type (WT) AR, the constitutively active ligand-binding mutant (Q640X), or DNA-binding mutants (C562S and G568W). **(H)** Schematic representation of luciferase reporter constructs containing the DUOX1 wild-type (WT, red), mutated (Mut, grey) ARE sites (altered residues shown in black), and an AR non-binding region (NB,

blue). **(I)** Bar plots showing luciferase reporter activity in DU145 cells transiently transfected with increasing concentrations of flag-tagged AR expression construct, in the presence of WT or Mut AREs and the NB region, as shown in (H). **(J)** Schematic representation of key structural domains of AR and the cloning strategy for wild-type (AR-WT) and a DNA-binding domain (DBD)-deleted mutant (AR-ΔDBD) in a flag-tagged expression vector. **(K)** Bar plots showing luciferase reporter activity in DU145 cells transiently transfected with AR-WT or AR-ΔDBD expression constructs, as shown in (J), in the presence of WT ARE. Data were presented as the mean ± SD, n ≥ 3 biological replicates. Significant differences were shown (** $p < 0.01$; *** $p < 0.001$; ns, not significant).

Figure 5

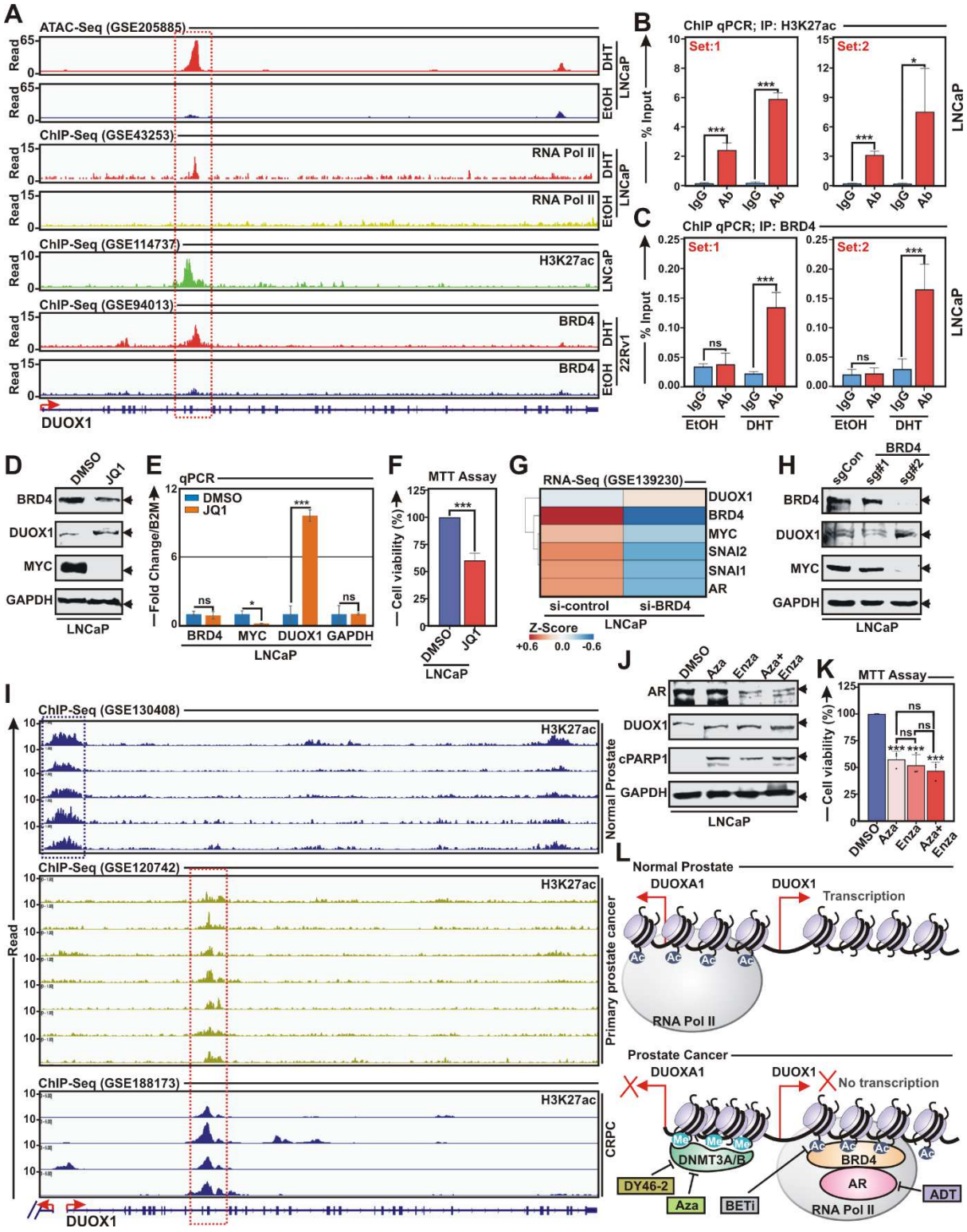


Figure 5. H3K27ac-BRD4 complex establishes a repressive chromatin circuit to suppress DUOX1 transcription. (A) ATAC-Seq (GSE205885) showing chromatin accessibility, along with ChIP-Seq tracks depicting enrichment of RNA polymerase II (RNA Pol II; GSE43253), H3K27ac (GSE114737), and BRD4 (GSE94013) signals at the intragenic enhancer region of the DUOX1 locus. **(B, C)** ChIP-qPCR analysis showing androgen-induced enrichment of (B) H3K27ac and (C) BRD4 at the AR-bound DUOX1 enhancer region in LNCaP cells. **(D)** WB analysis showing restoration of DUOX1 expression in LNCaP

cells following treatment with the BET inhibitor JQ1. **(E)** qPCR analysis showing relative expression of the indicated transcripts in LNCaP cells following JQ1 treatment, as in (D). **(F)** MTT assay demonstrating a significant reduction in viability of LNCaP cells upon JQ1 treatment. **(G)** Heatmap showing RNA-Seq analysis (GSE139230) following BRD4 knockdown, indicating increased DUOX1 expression accompanied by suppression of AR and MYC transcripts. **(H)** WB analysis of BRD4 knockout in LNCaP cells using two independent sgRNAs, showing increased DUOX1 expression upon efficient BRD4 depletion. **(I)** Reanalysis of H3K27ac ChIP-Seq datasets from normal prostate (GSE130408), primary PCa (GSE120742), and CRPC (GSE188173) samples, demonstrating redistribution of H3K27ac enrichment from the DUOX1 promoter to the AR-bound enhancer region during disease progression. **(J)** WB analysis showing DUOX1 expression in LNCaP cells following treatment with azacytidine (Aza), enzalutamide (Enza), or their combination. **(K)** MTT assay showing a reduction in the viability of LNCaP cells following treatment with the indicated drugs, administered either individually or in combination. **(L)** Working model illustrating DNMT3A/3B-mediated promoter hypermethylation and the H3K27ac-BRD4-AR-dependent repressive loop at the DUOX1 enhancer, along with reversal of this repression upon pharmacological inhibition. Data were presented as the mean ± SD, n ≥ 3 biological replicates. Significant differences were shown (*$p < 0.05$; *** $p < 0.001$; ns, not significant).

Figure 6

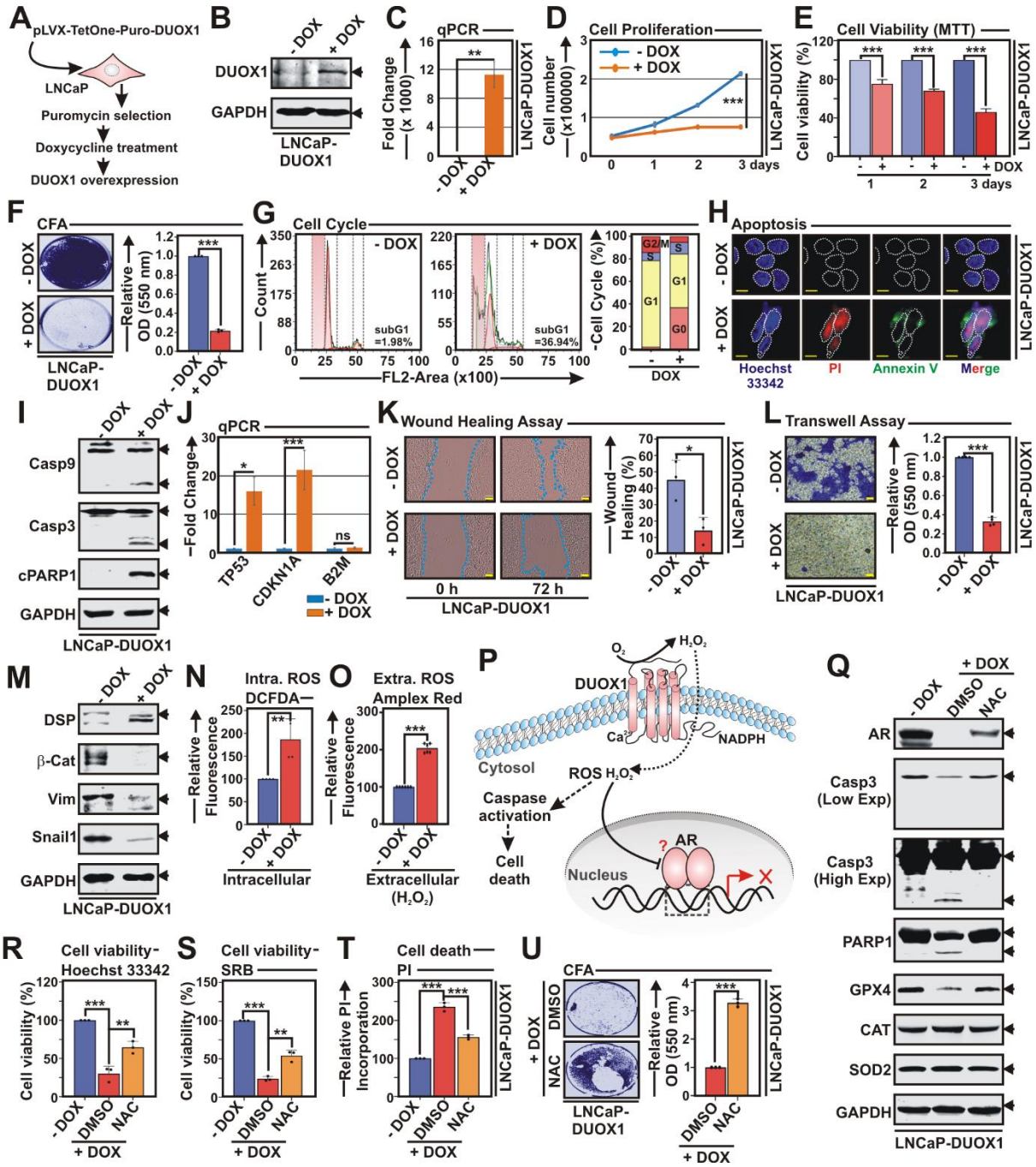


Figure 6. Ectopic DUOX1 expression in LNCaP cells suppresses proliferation and metastasis while promoting apoptotic cell death through extracellular ROS production. (A) Schematic representation of the generation of a doxycycline (DOX)-inducible DUOX1 stable expression system in LNCaP cells (LNCaP-DUOX1). **(B)** WB analysis validating DUOX1 protein expression in DOX-treated LNCaP-DUOX1 cells. **(C)** qPCR analysis confirming inducible DUOX1 expression upon DOX treatment in LNCaP-DUOX1 cells. **(D)** Cell proliferation assay using the Trypan Blue exclusion method showing reduced growth of LNCaP-DUOX1 cells upon DOX induction over time (0-3 days). **(E)** MTT assay showing decreased cell viability of LNCaP-DUOX1 cells following DUOX1 induction over time (0–3 days). **(F)** Colony formation assay (CFA) demonstrating reduced clonogenic potential in DUOX1-expressing LNCaP cells upon DOX induction, with quantification of Crystal Violet staining at 550 nm (right panel). **(G)** Flow cytometric analysis of cell cycle distribution indicating increased sub-G1 population upon DUOX1 expression in

LNCaP cells. **(H)** Immunofluorescence staining with propidium iodide (PI, red) and FITC-labeled Annexin V (green) demonstrating increased apoptosis in DUOX1-induced LNCaP cells. Nuclei were counterstained with Hoechst 33342 (blue). Scale bars, 5 µm. **(I)** WB analysis showing cleavage of apoptotic markers - Caspase-3, Caspase-7 and PARP upon DUOX1 induction in LNCaP cells. **(J)** qPCR analysis showing increased expression of TP53 and CDKN1A transcripts in DUOX1-expressing LNCaP cells. **(K)** Wound healing assay demonstrating reduced migratory capacity of DUOX1-expressing LNCaP cells upon DOX induction, with quantification (right panel). **(L)** Transwell invasion assay showing decreased invasive potential in DUOX1-expressing LNCaP cells, with quantification of Crystal Violet staining at 550 nm (right panel). **(M)** WB analysis showing differential expression of EMT markers upon DUOX1 induction in LNCaP cells. **(N)** DCFDA assay demonstrating increased intracellular ROS levels following DUOX1 expression in LNCaP cells. **(O)** Amplex Red assay showing elevated extracellular H_2O_2 production upon DUOX1 induction in LNCaP cells. **(P)** Schematic model illustrating DUOX1-mediated ROS generation, downstream apoptotic signaling, and potential regulation of AR activity. **(Q)** WB analysis showing differential expression of the indicated proteins in DUOX1-expressing LNCaP cells in the presence or absence of N-acetylcysteine (NAC). **(R-T)** Cell viability assays showing NAC-mediated rescue of cell death in DUOX1-expressing LNCaP cells using (R) Hoechst 33342 staining, (S) sulforhodamine B (SRB) assay, and (T) PI staining. **(U)** CFA demonstrating restoration of clonogenic potential in DUOX1-expressing LNCaP cells following NAC treatment, with quantification of Crystal Violet staining at 550 nm (right panel). Data were presented as the mean ± SD, n ≥ 3 biological replicates. Significant differences were shown (*$p < 0.05$; ** $p < 0.01$; *** $p < 0.001$; ns, not significant).

Figure 7

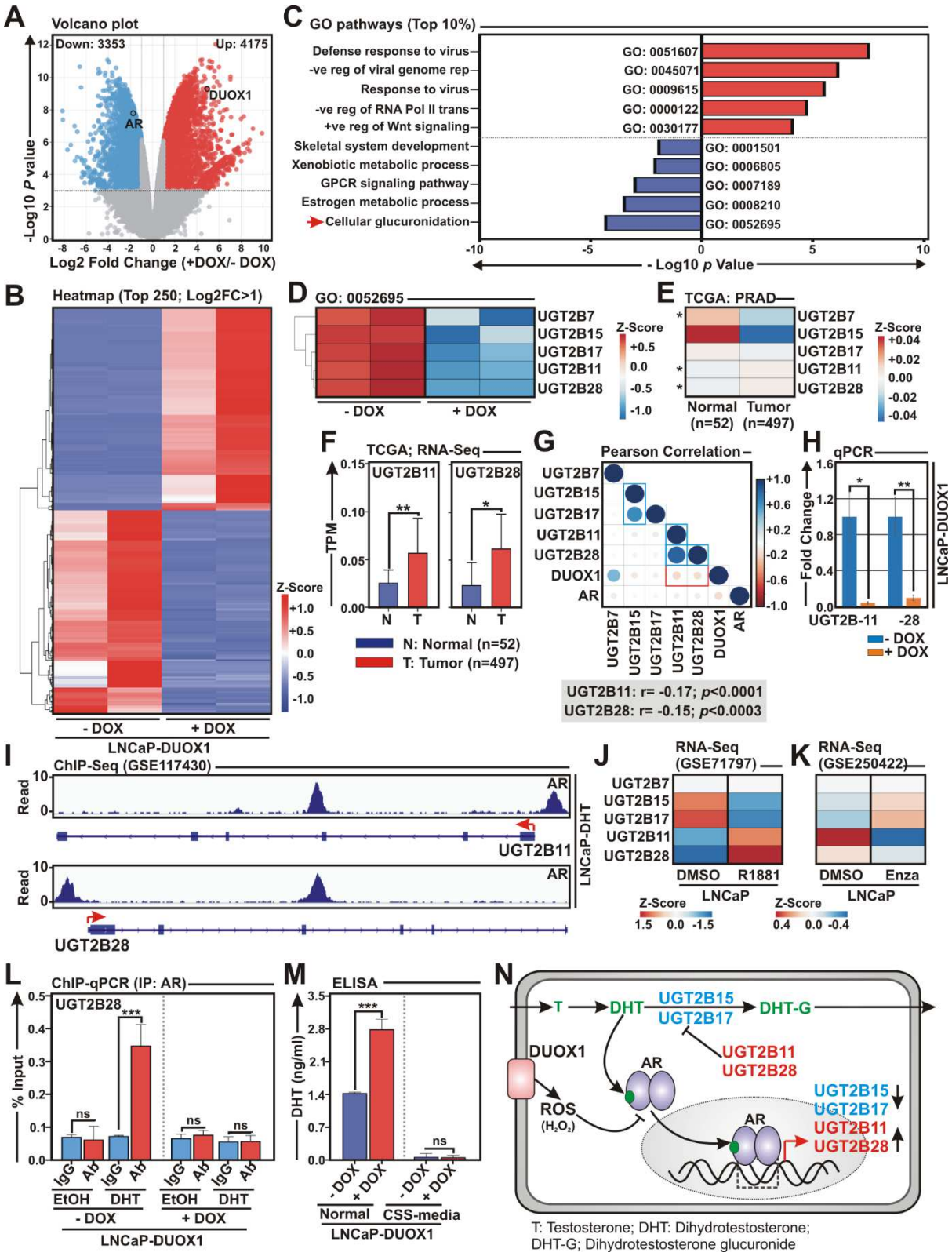


Figure 7. RNA-Seq analysis reveals DUOX1 overexpression profoundly deregulates glucuronidation pathway in androgen sensitive LNCaP cells. (A) Volcano plot depicting differentially expressed genes (DEGs) from bulk RNA-seq analysis of LNCaP-DUOX1 cells with or without DOX treatment (n=2), highlighting significantly upregulated (red) and downregulated (blue) transcripts. **(B)** Heatmap

showing hierarchical clustering of top 250 DEGs ($p < 0.001$, $|\log_2 FC| \geq 1$) between control and DUOX1-overexpressing LNCaP cells. **(C)** Gene Ontology (GO) and pathway enrichment analyses of top 10% DEGs, showing the top five significantly enriched pathways ($p < 0.05$); upregulated (red) and downregulated (blue). **(D)** Heatmap showing differential expression of five UDP-glucuronosyltransferase (UGT2B) family genes in control and DUOX1-overexpressing cells. **(E)** Heatmap showing differential expression of five UGT2B gene transcripts in normal and tumor samples from the TCGA-PRAD RNA-Seq dataset. **(F)** Bar plots showing expression of UGT2B11 and UGT2B28 in normal and tumor samples from the TCGA-PRAD RNA-Seq dataset. **(G)** Pearson correlation analysis demonstrating an inverse relationship between DUOX1 and UGT2B11 or UGT2B28 expression in the TCGA-PRAD RNA-Seq dataset. **(H)** qPCR analysis demonstrating reduced UGT2B11 and UGT2B28 transcript levels following DUOX1 expression in LNCaP cells. **(I)** AR ChIP-seq tracks (GSE117430) in LNCaP cells showing AR occupancy at the promoter regions of UGT2B11 (top) and UGT2B28 (bottom) following androgen stimulation with DHT. **(J, K)** Heatmaps showing relative mRNA expression of five UGT2B family members in RNA-seq datasets of LNCaP cells following (J) androgen stimulation with R1881 (GSE71797) or (K) androgen deprivation with enzalutamide (Enza; GSE250422). **(L)** ChIP-qPCR analysis demonstrating androgen-induced AR recruitment to the UGT2B28 promoter exclusively in the absence of DUOX1 expression. **(M)** Competitive ELISA for DHT showing increased extracellular DHT upon DUOX1 expression in LNCaP cells cultured in normal medium, whereas no detectable DHT was observed under charcoal-stripped serum (CSS) conditions. **(N)** Schematic model illustrating DUOX1-mediated disruption of glucuronidation pathways and its potential impact on androgen metabolism and AR signaling in PCa cells. Data were presented as the mean ± SD, n ≥ 3 biological replicates. Significant differences were shown (*$p < 0.05$; ** $p < 0.01$; *** $p < 0.001$; ns, not significant).

Supplementary Files

This is a list of supplementary files associated with this preprint. Click to download.

- OriginalData.pdf
- SupplementaryFiguresandTables.pdf
- DataSetS2.xlsx
- DataSetS1.xlsx